

A general fluid–sediment mixture model and constitutive theory validated in many flow regimes

Aaron S. Baumgarten¹ and Ken Kamrin^{2,†}

¹Department of Aeronautics and Astronautics, Massachusetts Institute of Technology, Cambridge, MA 02139, USA

²Department of Mechanical Engineering, Massachusetts Institute of Technology, Cambridge, MA 02139, USA

(Received 8 June 2018; revised 6 September 2018; accepted 5 November 2018;
first published online 28 December 2018)

We present a thermodynamically consistent constitutive model for fluid-saturated sediments, spanning dense to dilute regimes, developed from the basic balance laws for two-phase mixtures. The model can represent various limiting cases, such as pure fluid and dry grains. It is formulated to capture a number of key behaviours such as: (i) viscous inertial rheology of submerged wet grains under steady shearing flows, (ii) the critical state behaviour of grains, which causes granular Reynolds dilation/contraction due to shear, (iii) the change in the effective viscosity of the fluid due to the presence of suspended grains and (iv) the Darcy-like drag interaction observed in both dense and dilute mixtures, which gives rise to complex fluid–grain interactions under dilation and flow. The full constitutive model is combined with the basic equations of motion for each mixture phase and implemented in the material point method (MPM) to accurately model the coupled dynamics of the mixed system. Qualitative results show the breadth of problems which this model can address. Quantitative results demonstrate the accuracy of this model as compared with analytical limits and experimental observations of fluid and grain behaviours in inhomogeneous geometries.

Key words: granular media, multiphase and particle-laden flows, suspensions

1. Introduction

Mixtures of fluids and sediments play an important role in many industrial and geotechnical engineering problems, from transporting large volumes of industrial wastes to building earthen levees and dams. To solve these problems, engineers have traditionally relied on the myriad of empirical models developed in the last century. These empirical models are derived by coupling relevant experimental observations to an understanding of the underlying physics governing the behaviour of these mixtures. The model reported in Einstein (1906) describes the increase in effective fluid viscosity due to dilute suspensions of grains. The Darcy-like drag law given in

† Email address for correspondence: kkamrin@mit.edu

Carman (1937) describes the pressure drop in a fluid as it flows through a bed of densely packed grains. The work by Turian & Yuan (1977) characterizes the flow of slurries in pipelines. Other models (such as in Pailha & Pouliquen (2009)) describe more complex problems (such as the initiation of submerged granular avalanches); however, each of these models can only provide a description of a specific regime of mixture and flows.

To address an engineering problem that involves complex interactions of fluids and sediments spanning many flow regimes requires a more general modelling approach. A natural first step is to model the underlying physics directly by solving the coupled fluid–grain interactions at the micro-scale (as in the coupled lattice Boltzmann and discrete element method, LBM-DEM, proposed in Cook, Noble & Williams (2004)). Many problems of interest, however, involve far too much material for a direct approach to be computationally viable. We therefore turn to a continuum modelling approach, where the small-scale structures and physics are homogenized into bulk properties and behaviours.

Recent work simulating fluid–sediment mixtures as continua (see Soga *et al.* 2015) presents a versatile foundation, but the reported results are highly sensitive to the choice of sediment constitutive model (see Ceccato & Simonini 2016 and Fern & Soga 2016); even when pore pressure is uniform, no existing dry granular plasticity model correctly predicts the granular part of the rheology of saturated media. In this work, we carefully formulate a new set of constitutive rules governing the fluid and sediment phases of the continuum mixture. Using these rules, we construct a model that recovers the correct limiting behaviours – i.e. dry and viscous granular inertial rheologies, change of effective fluid viscosity due to suspended grains, Stokes and Carman–Kozeny drags and Reynolds dilation – and smoothly transitions between flow regimes covering the range from dense slurry-like flow to dilute suspensions. We implement our model in the material point method (MPM) and validate this implementation against several dynamic experiments involving submerged glass beads. We also consider the application of our model to the problems of slope collapse and intrusion.

2. Theory and formulation

Here we lay out the theoretical framework for the two-phase mixture model. In the formulation of this theory, we use the standard notation of continuum mechanics from Gurtin, Fried & Anand (2010). In particular, the trace of the tensor \mathbf{A} is given by $\text{tr } \mathbf{A}$ and the transpose by \mathbf{A}^\top . Every tensor admits the unique decomposition into a deviatoric part \mathbf{A}_0 and isotropic part by $\mathbf{A} = \mathbf{A}_0 + (1/3)\text{tr}(\mathbf{A})\mathbf{1}$ with $\mathbf{1}$ the identity tensor.

2.1. Mixture theory

To develop the model we start by considering a mixture of grains and fluid. We assume that the grains are rough (i.e. physical, frictional contact can occur between grains; see Zhao & Davis (2002)), made of incompressible material with true density ρ_s (i.e. the density of a grain) and essentially spherical with mean diameter d . Additionally, we assume that the grains are quasi-mono-disperse (no size segregation during flow) and that grains are large enough to neglect Brownian effects (i.e. $d \gtrsim 100 \mu\text{m}$ for common engineering slurries). We also assume that the grains are fully immersed in a barotropic viscous fluid having true density ρ_f and viscosity η_0 . We use the term ‘true’ to mean those properties of the material in the mixture before

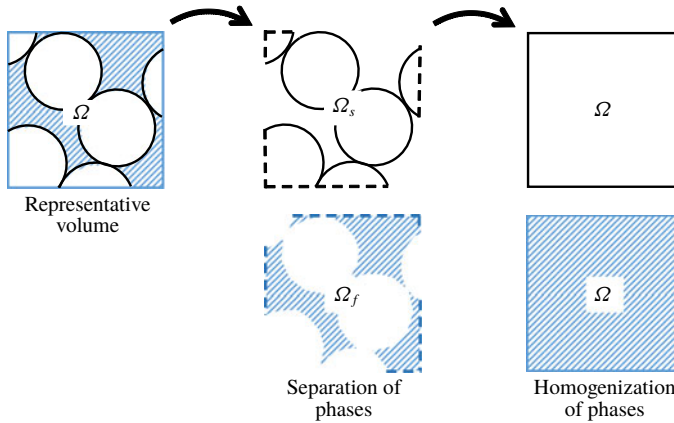


FIGURE 1. (Colour online) Pictorial description of the representative volume Ω , the decomposition of the domain into fluid and solid volumes, and the homogenization of the two phases.

the mixture is homogenized. A representative volume of material, Ω , can therefore be decomposed into a solid volume, Ω_s , and a fluid volume, Ω_f , such that $\Omega = \Omega_s \cup \Omega_f$.

Figure 1 shows how this volume is decomposed and the important step of homogenizing the solid volume and fluid volume into two, overlapping continua. In the analysis that follows, ψ_s will refer to some field ψ defined on the solid phase, and ψ_f will refer to some field ψ defined on the fluid phase. If no subscript is given, then that field is defined on the mixture as a whole.

2.1.1. Homogenization of phases

The effective densities, $\bar{\rho}_s$ and $\bar{\rho}_f$, and phase velocities, v_s and v_f , of the mixture are defined such that conservation of mass and momentum in the continuum correspond to conservation of mass and momentum in the real mixture. For this, we consider a representative volume of material, Ω , that contains a large number of individual grains. For the continuum approximation to be valid, large is defined such that grain-scale phenomena are smoothed out and bulk behaviour is captured. The volume of grains Ω_s and volume of fluid Ω_f within Ω allow us to define the solid phase volume fraction or packing fraction, ϕ , and a fluid phase volume fraction or porosity, n , as,

$$\bar{\rho}_s = \phi \rho_s, \quad \bar{\rho}_f = n \rho_f, \quad \text{with } \phi = 1 - n. \tag{2.1a,b}$$

The external body force acting on each homogenized phase (per unit volume), \mathbf{b}_{0s} and \mathbf{b}_{0f} , is proportional to the local effective density,

$$\mathbf{b}_{0s} = \bar{\rho}_s \mathbf{g}, \quad \mathbf{b}_{0f} = \bar{\rho}_f \mathbf{g}, \tag{2.2a,b}$$

where \mathbf{g} is the gravitational acceleration vector.

We next define the mixture Cauchy stress, $\boldsymbol{\sigma}$, according to Cauchy’s theorem such that the stress response of the mixture is expressed as the sum of the phase-wise effective Cauchy stresses, $\boldsymbol{\sigma}_s$ and $\boldsymbol{\sigma}_f$, i.e.

$$\boldsymbol{\sigma} = \boldsymbol{\sigma}_s + \boldsymbol{\sigma}_f. \tag{2.3}$$

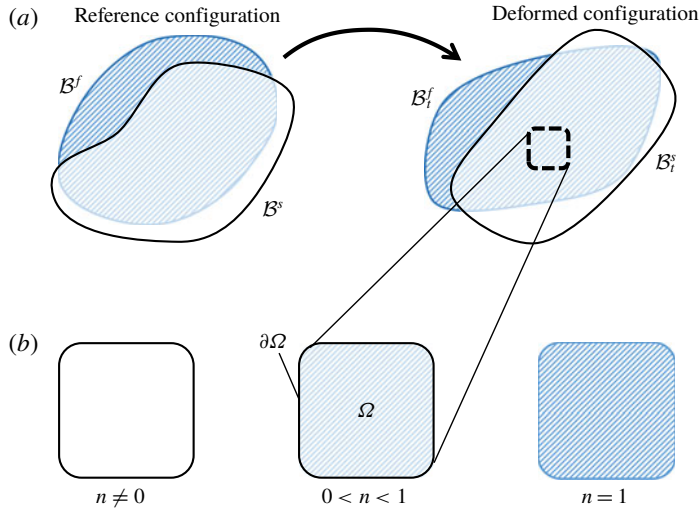


FIGURE 2. (Colour online) (a) Pictorial definition of the reference bodies, \mathcal{B}^s and \mathcal{B}^f , and deformed bodies, \mathcal{B}_t^s and \mathcal{B}_t^f . (b) Parts in the deformed body are always fully saturated with porosity $n > 0$. In the limit of a fluid-only volume, the porosity $n = 1$. In the limit of a solid-only volume, we do not let the porosity n go to zero, instead we let the fluid viscosity, bulk modulus and true density go to zero which effectively removes the fluid by making it stress and density free.

2.1.2. Overlapping continuum bodies

When considering a mixture problem, we begin by defining each phase as its own continuum body, as shown in figure 2(a). \mathcal{B}^s defines the initial solid phase body (or reference body) and \mathcal{B}^f defines the fluid phase reference body. At some later time t , these bodies are represented by \mathcal{B}_t^s and \mathcal{B}_t^f .

To determine the behaviour of a volume of mixture Ω , as shown in figure 2(b), we let that volume define a part in each continuum body. The full mixture is defined by the sum of these parts. If the volume of mixture is composed of fluid only, the porosity n is unity. We also enforce that, in the absence of a solid phase, the local solid phase stress is zero, $\sigma_s = \mathbf{0}$. In this limit, we expect the behaviour of the mixture to be identical to that of a barotropic viscous fluid on its own. If the volume of mixture is solid only, the porosity n is not zero (it would only be zero in the limit of vanishing pore space between grains). In this limit, the behaviour of the mixture should be identical to that of a dry granular material. To ensure this, we enforce that the local fluid phase stress is zero, $\sigma_f = \mathbf{0}$, and that the true fluid density, ρ_f , vanishes.

2.1.3. Mass conservation

We now define the equations governing the evolution of the true fluid density (i.e. the density of the fluid that is between the grains), ρ_f , and the effective densities of both phases, $\bar{\rho}_s$ and $\bar{\rho}_f$. Recalling that the solid grains are assumed to be incompressible, ρ_s is constant. However, $\bar{\rho}_s$ changes when the solid phase compacts or dilates as the structure of the granular skeleton changes. Since we will often have fields which belong to one phase or another (e.g. ρ_s belongs to the solid phase), it is convenient to define the material derivatives on each phase as

follows,

$$\frac{D^s \psi}{Dt} = \frac{\partial \psi}{\partial t} + \mathbf{v}_s \cdot \text{grad } \psi, \quad \frac{D^f \psi}{Dt} = \frac{\partial \psi}{\partial t} + \mathbf{v}_f \cdot \text{grad } \psi. \quad (2.4a,b)$$

Mass conservation in a part of the solid phase continuum (as defined by a volume Ω) is enforced by setting the material derivative of solid mass in the volume to zero. As shown in Bandara & Soga (2015), this requires that,

$$\frac{D^s \bar{\rho}_s}{Dt} + \bar{\rho}_s \text{div } \mathbf{v}_s = 0. \quad (2.5)$$

A simple expansion of this expression using the definition of porosity from (2.1) yields an expression for the rate of change of the local measure of porosity,

$$\frac{\partial n}{\partial t} = (1 - n) \text{div } \mathbf{v}_s - \mathbf{v}_s \cdot \text{grad } n. \quad (2.6)$$

Mass conservation of a fluid part defined by the arbitrary volume Ω is enforced by,

$$\frac{D^f \bar{\rho}_f}{Dt} + \bar{\rho}_f \text{div } \mathbf{v}_f = 0. \quad (2.7)$$

Combining (2.7) with (2.1) and (2.6), we find the correct form of the evolution law for the true fluid density,

$$\frac{n}{\rho_f} \frac{D^f \rho_f}{Dt} = -\text{div} ((1 - n)\mathbf{v}_s + n\mathbf{v}_f). \quad (2.8)$$

2.1.4. Momentum balance

Conservation of linear momentum is enforced locally for the each continuum body (see figure 2) as follows,

$$\left. \begin{aligned} \bar{\rho}_s \frac{D^s \mathbf{v}_s}{Dt} &= \mathbf{b}_{0s} - \mathbf{f}_b - \mathbf{f}_d + \text{div } \boldsymbol{\sigma}_s \\ \bar{\rho}_f \frac{D^f \mathbf{v}_f}{Dt} &= \mathbf{b}_{0f} + \mathbf{f}_b + \mathbf{f}_d + \text{div } \boldsymbol{\sigma}_f, \end{aligned} \right\} \quad (2.9)$$

where \mathbf{f}_b and \mathbf{f}_d are inter-phase body forces. \mathbf{f}_d is the inter-phase drag or Darcy’s law force. \mathbf{f}_b has the form of the buoyant force described in Drumheller (2000) for immiscible mixtures,

$$\mathbf{f}_b = p_f \text{grad } (n). \quad (2.10)$$

We let the solid phase stress $\boldsymbol{\sigma}_s$ take the classic form,

$$\boldsymbol{\sigma}_s = \tilde{\boldsymbol{\sigma}} - (1 - n)p_f \mathbf{1}. \quad (2.11)$$

The effective granular stress $\tilde{\boldsymbol{\sigma}}$ is the portion of the solid phase stress resulting from granular contact forces and from microscopic viscous stresses on grains from the fluid medium; it excludes the pressurization of the grains due to the pressure of the pore fluid. When the solid phase is dense, this also describes the Terzaghi effective stress that governs plastic flow of the solid phase. The term p_f is the true fluid phase pore pressure. Since the fluid is barotropic, this is determined by the true fluid density ρ_f .

The expression for the fluid phase stress $\boldsymbol{\sigma}_f$ is,

$$\boldsymbol{\sigma}_f = \boldsymbol{\tau}_f - np_f \mathbf{1}. \quad (2.12)$$

The fluid phase stress is decomposed into a deviatoric part, $\boldsymbol{\tau}_f$, (i.e. $\text{tr}(\boldsymbol{\tau}_f) = 0$) and an isotropic part, $np_f \mathbf{1}$. With the expressions for the stresses and the buoyant body force given in (2.11), (2.12) and (2.10), we recover the equations of motion from Jackson (2000).

The solid phase equation of motion is given as,

$$\bar{\rho}_s \frac{D^s \mathbf{v}_s}{Dt} = \bar{\rho}_s \mathbf{g} - \mathbf{f}_d + \text{div}(\tilde{\boldsymbol{\sigma}}) - (1-n) \text{grad}(p_f) \quad (2.13)$$

and the fluid phase equation of motion is given as,

$$\bar{\rho}_f \frac{D^f \mathbf{v}_f}{Dt} = \bar{\rho}_f \mathbf{g} + \mathbf{f}_d + \text{div}(\boldsymbol{\tau}_f) - n \text{grad}(p_f). \quad (2.14)$$

The equations in (2.13) and (2.14) fully describe the motion and behaviour of the mixture; however, we still need to define the specific rules governing the viscous drag between the phases \mathbf{f}_d , the elastic–plastic behaviour of the solid phase $\tilde{\boldsymbol{\sigma}}$, the pore fluid pressure p_f and the viscous shear response of the fluid phase $\boldsymbol{\tau}_f$. By carefully defining these four constitutive rules, we capture the rheologically correct behaviour for mixtures of fluid and grains.

2.1.5. First and second laws of thermodynamics

To formulate the rules for \mathbf{f}_d , $\tilde{\boldsymbol{\sigma}}$, p_f and $\boldsymbol{\tau}_f$, we start by defining the thermodynamic laws governing our mixture. When considering a single phase of material, it is often useful to assume that internal energy (ε), entropy (s) and absolute temperature (ϑ) are basic properties of a material. That is, they do not need to be defined in terms of other more basic properties. For our mixture model, we assume that analogous continuum fields exist describing the energy, entropy and temperature of the two continuum phases; however the physical basis of these fields is poorly defined (see Wilmanski 2008 and Klika 2014). We therefore rely on the intuition developed in Gurtin *et al.* (2010) to specialize the thermodynamic analysis from Drumheller (2000) to a mixture of grains (represented by an elastic–plastic porous solid) with a barotropic viscous fluid.

The full thermodynamic analysis is shown in appendix A, and a brief summary of the resulting constitutive rules is given in table 1. Through the analysis, we find that the fluid pore pressure p_f must be defined by the fluid phase specific free energy function $\hat{\psi}_f(\rho_f)$ and that the fluid shear stress $\boldsymbol{\tau}_f$ and inter-phase drag \mathbf{f}_d must both be dissipative, that is they must ‘resist’ their driving motion (the symmetric part of the fluid phase velocity gradient \mathbf{D}_f and the difference in phase velocities ($\mathbf{v}_s - \mathbf{v}_f$) respectively). We also show that the solid phase effective granular stress $\tilde{\boldsymbol{\sigma}}$ can be expressed as that of an elastic–plastic solid with behaviour defined by (A 22). For these kinds of materials, the stress is determined by the strain–energy function $\hat{\phi}_s$, which depends on the elastic part of the deformation gradient \mathbf{F}^e as defined in (A 13), which in turn defines the elastic volume Jacobian J^e and the right elastic Cauchy–Green tensor \mathbf{C}^e . The elastic tensor \mathbf{F}^e is a history dependent material tensor that evolves through time according to a decomposition of the solid phase strain rate \mathbf{D}_s into an elastic strain rate \mathbf{D}^e and a plastic part $\tilde{\mathbf{D}}^p$ according to (B 7) and

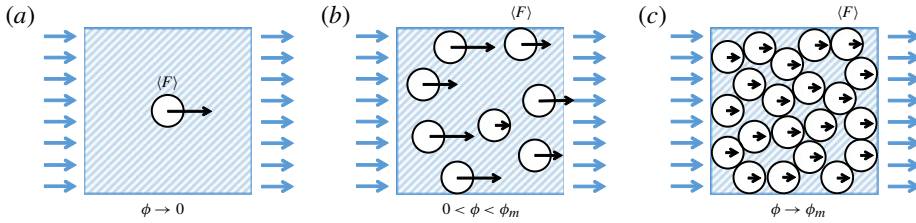


FIGURE 3. (Colour online) The three regimes over which the inter-phase drag f_d must be defined. The normalized average drag force $\langle F \rangle$ is taken from van der Hoef, Beetstra & Kuipers (2005) to be the average force on a single grain for a given packing fraction ϕ at a given flow rate.

Rule	Expression	Number
Fluid pore pressure equality	$p_f - \rho_f^2 \frac{\partial \hat{\psi}_f(\rho_f)}{\partial \rho_f} = 0$	(A 20)
Fluid shear stress inequality	$\boldsymbol{\tau}_f : \mathbf{D}_f \geq 0$	(A 21)
Effective granular stress equality	$\tilde{\boldsymbol{\sigma}} - 2J^{e-1} \mathbf{F}^e \frac{\partial \hat{\psi}_s(\mathbf{C}^e)}{\partial \mathbf{C}^e} \mathbf{F}^{e\top} = 0$	(A 22)
Effective granular stress inequality	$\tilde{\boldsymbol{\sigma}} : \tilde{\mathbf{D}}^p - J^{e-1} \varphi_s \text{tr}(\tilde{\mathbf{D}}^p) \geq 0$	(A 23)
Drag law inequality	$\mathbf{f}_d \cdot (\mathbf{v}_s - \mathbf{v}_f) \geq 0$	(A 24)

TABLE 1. Summary of thermodynamic rules for constitutive laws derived in appendix A.

subject to the dissipative inequality in (A 23). We note that in most common granular materials the bulk elastic deformations are extremely small, especially compared to plastic deformation, however grains do have finite stiffness and proper accounting of granular elasticity is important for thermodynamic consistency of the constitutive relations.

2.2. Inter-phase drag law

The flow of a viscous fluid around and between grains of sediment will result in an inter-phase drag that we represent with the drag force \mathbf{f}_d . This drag force can be understood as a body force acting on one phase by the other and has units N m^{-3} . In this work we assume that this force depends only on the relative velocities of the two phases $(\mathbf{v}_s - \mathbf{v}_f)$, the porosity of the mixture n , the grain diameter d and the fluid viscosity η_0 . We neglect dependence on material orientation or rotation (e.g. a fabric tensor) and neglect the effects of tortuosity (see Coussy 2004) on the apparent inter-phase drag.

For small flow velocities, the drag interaction between the fluid and the solid grains in the dilute limit shown in figure 3(a) is given analytically by the Stokes–Einstein equation.

$$\langle F \rangle = 3\pi\eta_0 du, \tag{2.15}$$

where u is the free-stream flow speed. ‘Small’ here is taken to mean $Re \rightarrow 0$ with,

$$Re \equiv \frac{n\rho_f d \|\mathbf{v}_s - \mathbf{v}_f\|}{\eta_0}. \tag{2.16}$$

The leading n in (2.16) is taken from Dupuit (1863) and relates the free-stream velocity to the average pore velocity. Normalizing the inter-phase drag by the volume average of the Stokes–Einstein drag on a single grain suggests the following functional form of f_d ,

$$f_d = \frac{18\phi(1-\phi)\eta_0}{d^2} \hat{F}(\phi, Re)(\mathbf{v}_s - \mathbf{v}_f), \quad (2.17)$$

with $\hat{F}(\phi, Re)$ a function of non-dimensional parameters only. The only thermodynamic requirement on f_d (see (A 24)) is satisfied if $\hat{F}(\phi, Re) \geq 0$ for all values of ϕ and Re .

Determining the expression for $\hat{F}(\phi, Re)$ for the full range of potential packing fractions ($0 \leq \phi \lesssim 0.65$) has historically been an intractable challenge. Analytical methods cannot be used for high Reynolds number flows ($Re > 1$) and flows with non-negligible packing fractions ($\phi > 0$) (see Clift, Grace & Weber 2005). Experimentally, any loose packing ($\phi \lesssim 0.58$) without sustained granular contacts will quickly compact, making the collection of accurate measurements near impossible.

Recent work by van der Hoef *et al.* (2005) and Beetstra, van der Hoef & Kuipers (2007) make use of the lattice-Boltzmann method to simulate the flow of fluid around mono- and bi-disperse packings of spheres for $0.10 < \phi < 0.6$ and $Re < 1000$. These simulations give the following form of \hat{F} at low Reynolds numbers ($Re \rightarrow 0$),

$$\hat{F}(\phi, 0) = \frac{10\phi}{(1-\phi)^2} + (1-\phi)^2(1 + 1.5\sqrt{\phi}), \quad (2.18)$$

with the following high Reynolds number correction,

$$\hat{F}(\phi, Re) = \hat{F}(\phi, 0) + \frac{0.413Re}{24(1-\phi)^2} \left(\frac{(1-\phi)^{-1} + 3\phi(1-\phi) + 8.4Re^{-0.343}}{1 + 10^{3\phi}Re^{-(1+4\phi)/2}} \right). \quad (2.19)$$

In the dilute, low Reynolds number limit, (2.18) and (2.19) recover the Stokes–Einstein inter-phase drag. In the dense, low Reynolds number limit, (2.18) and (2.19) recover the Carman–Kozeny inter-phase drag from Carman (1937) as used in Bandara & Soga (2015),

$$\lim_{\phi \rightarrow 0} \hat{F}(\phi, 0) = 1, \quad \lim_{\phi \rightarrow 1} \hat{F}(\phi, 0) = \frac{10\phi}{(1-\phi)^2}. \quad (2.20a,b)$$

2.3. Fluid phase pore pressure

The fluid phase pore pressure is governed by the constitutive relation given in (A 20). We let the fluid phase free energy function, $\hat{\psi}(\rho_f)$, be given by,

$$\hat{\psi}_f(\rho_f) = \kappa \left(\frac{\ln(\rho_{0f}) - \ln(\rho_f) - 1}{\rho_f^2} \right), \quad \text{such that } p_f = \kappa \ln \left(\frac{\rho_f}{\rho_{0f}} \right), \quad (2.21a,b)$$

where ρ_{0f} is the true fluid density for which $p_f = 0$ and κ is the fluid bulk modulus with units of Pa.

2.4. *Fluid phase shear stress*

We assume that the functional form of $\boldsymbol{\tau}_f$ is given by, $\boldsymbol{\tau}_f = \hat{\boldsymbol{\tau}}_f(\mathbf{D}_f, \phi)$ with $\hat{\boldsymbol{\tau}}_f$ isotropic and linear in \mathbf{D}_f , the symmetric part of the fluid strain-rate tensor (see (A 9a,b)). From Truesdell & Noll (1965), the representation theorem for isotropic linear tensor functions requires that

$$\hat{\boldsymbol{\tau}}_f(\mathbf{D}_f, \phi) = 2\mu(\phi)\mathbf{D}_f + \lambda(\phi)\text{tr}(\mathbf{D}_f)\mathbf{1}. \tag{2.22}$$

We assume $\boldsymbol{\tau}_f$ is deviatoric, which requires $\lambda(\phi) = -(2/3)\mu(\phi)$. And the thermodynamic restriction on $\boldsymbol{\tau}_f$ in (A 21) yields $\mu(\phi) \geq 0$. We let the effective fluid phase viscosity, $\mu(\phi)$, be given by the linear relation from Einstein (1906) such that,

$$\boldsymbol{\tau}_f = 2\eta_0 \left(1 + \frac{5}{2}\phi\right) \mathbf{D}_{0f}, \tag{2.23}$$

with η_0 defined previously as the true fluid viscosity.

2.5. *Solid phase stress evolution*

The solid phase effective granular stress is a function of the accumulated elastic deformation in the solid phase, \mathbf{F}^e , as defined in (A 22) (see table 1). In appendix B, we show that for stiff elastic materials, (A 22) is satisfied if the effective granular stress is evolved according to the following approximation using the Jaumann objective rate of $\tilde{\boldsymbol{\sigma}}$,

$$\overset{\Delta}{\tilde{\boldsymbol{\sigma}}} \equiv \frac{D^s \tilde{\boldsymbol{\sigma}}}{Dt} - \mathbf{W}_s \tilde{\boldsymbol{\sigma}} + \tilde{\boldsymbol{\sigma}} \mathbf{W}_s \approx \mathcal{C}[\mathbf{D}^e], \tag{2.24}$$

with \mathcal{C} an elastic stiffness tensor defined in (B 4), \mathbf{W}_s the skew part of the solid phase velocity gradient and $\mathbf{D}^e = \mathbf{D}_s - \tilde{\mathbf{D}}^p$ (see (B 7)). The material derivative of the effective granular stress is therefore given by,

$$\frac{D^s \tilde{\boldsymbol{\sigma}}}{Dt} = 2G\mathbf{D}^{e0} + K\text{tr}(\mathbf{D}^e)\mathbf{1} + \mathbf{W}_s \tilde{\boldsymbol{\sigma}} - \tilde{\boldsymbol{\sigma}} \mathbf{W}_s. \tag{2.25}$$

In this way, we evolve the effective granular stress according to how the solid phase is straining (\mathbf{D}_s) minus how much of that strain rate is plastic ($\tilde{\mathbf{D}}^p$). Physically, when the solid phase is flowing, most of the strain is accumulated plastically; when the solid phase is static (or resisting flow), strain is accumulated elastically. In this sense, through careful selection of the plastic flow rule $\tilde{\mathbf{D}}^p$, the model can represent both flowing and static (sub-yield) behaviours of the solid phase.

2.6. *Solid phase plastic flow rules*

We let $\tilde{\mathbf{D}}^p$ have the following form,

$$\tilde{\mathbf{D}}^p = \frac{\dot{\gamma}^p}{\sqrt{2}} \frac{\tilde{\boldsymbol{\sigma}}_0}{\|\tilde{\boldsymbol{\sigma}}_0\|} + \frac{1}{3}(\beta\dot{\gamma}^p + \dot{\xi}_1 + \dot{\xi}_2)\mathbf{1}, \tag{2.26}$$

where the ‘over-dot’ operator $\dot{\psi}$ is equivalent to the material derivative $D^s \psi / Dt$. The only thermodynamic constraint on this plastic flow relation is given by (B 8). It is a simple exercise to show that the following formulation obeys that inequality.

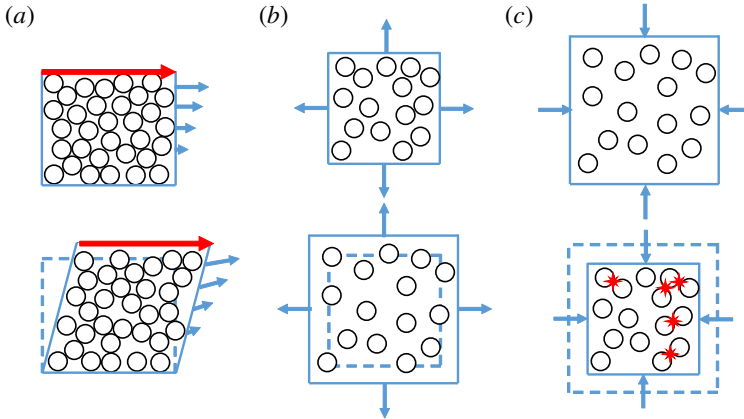


FIGURE 4. (Colour online) (a) In shear, the granular phase will obey critical state behaviour. This phenomenon is called Reynolds' dilation and is captured by the rate of plastic dilation, $\beta \dot{\gamma}^p$. (b) In expansion, the granular phase will come apart freely. This phenomenon is stress free and is captured by the rate of plastic expansion, $\dot{\xi}_1$. (c) In compaction, granular collisions will result in a macroscopic pressure. This phenomenon is governed by the rate of plastic compaction, $-\dot{\xi}_2$.

The equivalent plastic shear strain rate $\dot{\gamma}^p$, the rate of plastic expansion $\dot{\xi}_1$ (figure 4b), the rate of plastic compaction $-\dot{\xi}_2$ (figure 4c) and the rate of Reynolds dilation $\beta \dot{\gamma}^p$ (figure 4a) are the scalar measures that give the solid phase plastic flow. These flow measures are uniquely determined by the solid phase strain rate \mathbf{D}_s , the solid phase effective stress $\tilde{\sigma}$ and the current state of the mixture.

The dilation angle, β , governs the rate of Reynolds dilation during plastic shear (see Rudnicki & Rice 1975; Roux & Radjai 1998 and Roux & Radjai 2001) and allows the material to dilate when shearing over-compacted grains and contract when shearing under-compacted grains. We use the functional form of β given in Pailha & Pouliquen (2009),

$$\beta = K_3(\phi - \phi_{eq}), \quad (2.27)$$

where K_3 is a unit-less material parameter and ϕ_{eq} is the rate-dependent equilibrium packing fraction achieved in steady-state shearing, given by Amarsid *et al.* (2017) as,

$$\phi_{eq} = \frac{\phi_m}{1 + aI_m}, \quad (2.28)$$

with a a material parameter, I_m the mixed inertial number and ϕ_m a material parameter describing the maximum possible packing fraction for a granular material in steady-state shearing flow. The non-dimensional inertial numbers (including the inertial number, I , and the viscous inertial number, I_v) are defined as,

$$I = \dot{\gamma}^p d \sqrt{\frac{\rho_s}{\tilde{p}}}, \quad I_v = \frac{\eta_0 \dot{\gamma}^p}{\tilde{p}}, \quad I_m = \sqrt{I^2 + 2I_v}, \quad (2.29a-c)$$

with \tilde{p} the granular pressure described in Boyer, Gauzelli & Pouliquen (2011). The specific form of the mixed inertial number, I_m , was determined in Amarsid *et al.* (2017) by analysing numerous two-dimensional shearing flows spanning the inertial and viscous regimes ($0 \lesssim I \lesssim 0.1$ and $0 \lesssim I_v \lesssim 0.2$).

To determine $\dot{\gamma}^p$, $\dot{\xi}_1$ and $\dot{\xi}_2$ it is convenient to express their functional dependences implicitly in terms of the yield conditions given below. First, we uniquely define the equivalent plastic shear rate $\dot{\gamma}^p$ by solving

$$\left. \begin{aligned} f_1 &= \bar{\tau} - \max((\mu_p + \beta)\tilde{p}, 0) \\ f_1 &\leq 0, \quad \dot{\gamma}^p \geq 0, \quad f_1 \dot{\gamma}^p = 0, \end{aligned} \right\} \tag{2.30}$$

with,

$$\bar{\tau} = \frac{\|\tilde{\sigma}_0\|}{\sqrt{2}}, \quad \tilde{p} = -\frac{1}{3}\text{tr}(\tilde{\sigma}). \tag{2.31a,b}$$

Solutions to this system have non-zero plastic shearing only when the yield condition, $f_1 = 0$, is met, and vanishing plastic shear rate when below yield, $f_1 < 0$. We let $\mu_p = \hat{\mu}_p(\phi, I_v, I_m)$, which is formulated to capture both the $\mu(I)$ dry granular rheology from Jop, Forterre & Pouliquen (2006) and the $\mu(I_v)$ low Stokes mixture rheology from Boyer *et al.* (2011), as will be shown in § 3. The functional form of $\hat{\mu}_p$ is defined as,

$$\hat{\mu}_p(\phi, I_v, I_m) = \mu_1 + \frac{\mu_2 - \mu_1}{1 + (b/I_m)} + \frac{5}{2} \left(\frac{\phi I_v}{a I_m} \right). \tag{2.32}$$

Note that in steady-state shearing, $\phi = \phi_{eq}$ and $\hat{\mu}_p$ reduces to a function of I_v and I_m only.

Granular separation, represented by the rate of plastic expansion, $\dot{\xi}_1$, is obtained from the conditions

$$\left. \begin{aligned} f_2 &= -\tilde{p} \\ f_2 &\leq 0, \quad \dot{\xi}_1 \geq 0, \quad f_2 \dot{\xi}_1 = 0. \end{aligned} \right\} \tag{2.33}$$

These conditions enforce the assumption that non-cohesive grains cannot support tension. Hence, the granular media undergoes plastic expansion $\dot{\xi}_1$, representing grain separation, in lieu of developing tensile granular stress states.

The flow rule governing plastic compaction, $-\dot{\xi}_2$, arises from solving the system below:

$$\left. \begin{aligned} f_3 &= g(\phi)\tilde{p} - (a\phi)^2 [(\dot{\gamma}^p - K_4 \dot{\xi}_2)^2 d^2 \rho_s + 2\eta_0(\dot{\gamma}^p - K_4 \dot{\xi}_2)] \\ f_3 &\leq 0, \quad \dot{\xi}_2 \leq 0, \quad f_3 \dot{\xi}_2 = 0, \end{aligned} \right\} \tag{2.34}$$

with,

$$g(\phi) = \begin{cases} (\phi_m - \phi)^2 & \text{if } \phi < \phi_m \\ 0 & \text{if } \phi \geq \phi_m. \end{cases} \tag{2.35}$$

The form of $g(\phi)$ and the f_3 yield surface are chosen such that, when the material is being compacted or sheared but is less dense than the critical packing, $\phi < \phi_m$, there is an upper bound on the admissible effective pressure \tilde{p} . However, in the compacted regime, $\phi \geq \phi_m$, any pressure is admissible, as the grains are assumed to always be touching. The upper bound on the value of \tilde{p} is determined by inverting the expression for ϕ_{eq} defined in (2.28). The unit-less K_4 coefficient defines the relative importance of the plastic compaction rate in determining this upper bound compared to the plastic shear rate.

Together (2.25), (2.26), (B 7), (2.30), (2.33) and (2.34) uniquely determine the plastic flow rates $\dot{\gamma}^p$, $\dot{\xi}_1$ and $\dot{\xi}_2$. It is also important to note that the specific forms of (2.33) and (2.34) restrict $\dot{\xi}_1$ to be zero when plastic compaction occurs and restrict $\dot{\xi}_2$ to be zero when plastic expansion occurs.

2.7. Summary of model assumptions

The model presented in this section is formulated to capture several key phenomena observed in mixtures of fluids and grains. In the development of this model we have assumed that the granular material is quasi-mono-disperse, composed of incompressible cohesion-less solid grains, and fully saturated with an isothermal Newtonian liquid. We have neglected Brownian effects on the mixture, limiting the applicability of our model to the study of granular mixtures which are dominated by gravitational energy or by shearing time scales ($d \gtrsim 100 \mu\text{m}$ for common engineering slurries). In addition, the evolution law for the effective granular stress (including the plastic flow rule) is only applicable in the limit of stiff elasticity ($G, K \gg \tilde{p}$).

We have derived our inter-phase drag law (see (2.17)) from the empirical relations given in Carman (1937), van der Hoef *et al.* (2005) and Beetstra *et al.* (2007). The simulations and experiments that underpin these empirical relations suggest that this drag law is applicable for $0 \leq \phi \lesssim 0.65$ and $Re \leq 1000$. In addition the internal friction coefficient for the solid phase (see (2.32)) is developed through consideration of models presented in Stickel & Powell (2005), Boyer *et al.* (2011) and Amarsid *et al.* (2017). The data which underpin these empirical models suggest that the internal friction model is applicable for $I \lesssim 0.2$, $I_v \lesssim 0.1$, $I_m \lesssim 0.6$ and $0 \leq St < \infty$.

3. Analytical verification of model

In this section we verify that the model laid out in §2 has the correct limiting behaviour in a simple shearing flow. In particular we are interested in showing that under the appropriate conditions, the following rheologies are captured.

- (i) $\mu(I)$, $\phi(I)$ steady-state dry granular inertial rheology.
- (ii) $\mu(I_v)$, $\phi(I_v)$ steady-state viscous inertial rheology.
- (iii) $\eta_r(\phi)$ slurry/suspension effective viscosity.

These phenomena should arise as different cases of steady shearing flow wherein the mixture is co-moving such that, $\mathbf{v}_s = \mathbf{v}_f$ and,

$$\text{grad}(\mathbf{v}_s) = \text{grad}(\mathbf{v}_f) = \mathbf{L} = \begin{bmatrix} 0 & \dot{\gamma} & 0 \\ 0 & 0 & 0 \\ 0 & 0 & 0 \end{bmatrix}, \quad (3.1)$$

where $\dot{\gamma}$ is the applied steady shear rate. Since the mixture is uniform and $\text{tr}(\mathbf{L}) = 0$, (2.8) tells us that the true fluid density, ρ_f , is constant. By (2.21), this means that the fluid phase pore pressure remains constant, $p_f = p_{eq}$, with p_{eq} some constant equilibrium pressure.

The fluid phase shear stress, $\boldsymbol{\tau}_f$, is determined by (2.23),

$$\boldsymbol{\tau}_f = \eta_0 \left(1 + \frac{5}{2} \phi \right) \begin{bmatrix} 0 & \dot{\gamma} & 0 \\ \dot{\gamma} & 0 & 0 \\ 0 & 0 & 0 \end{bmatrix}. \quad (3.2)$$

In the solid phase, there are two regimes of interest, the compacted regime with $\phi \geq \phi_m$ and the non-compacted regime with $\phi < \phi_m$. In the compacted regime, the sustained granular contacts result in non-steady behaviour (the positivity of the dilatation angle β from (2.27) results in continuous growth of the pressure \tilde{p}). For this reason, we will be more interested in the behaviour of the non-compacted regime, where steady-state flow is possible.

Assuming that the solid phase begins in a stress-free state and that the shear modulus, G , is much greater than the characteristic shear stress, it can be shown that (2.25) and (2.26) together imply that $\tilde{\sigma}$ will reach a steady value with the equivalent plastic shear rate $\dot{\gamma}^p$ non-zero and equivalent to the total steady shear rate $\dot{\gamma}$. The solid phase effective granular stress then satisfies,

$$\tilde{\sigma} \approx \begin{bmatrix} \tilde{p} & \mu_p \tilde{p} & 0 \\ \mu_p \tilde{p} & \tilde{p} & 0 \\ 0 & 0 & \tilde{p} \end{bmatrix}. \tag{3.3}$$

The total mixture stress as defined in (2.3) is characterized by the mixture pressure $p = -(1/3)\text{tr}(\sigma)$ and the mixture shear stress $\tau = (1/\sqrt{2})\|\sigma_0\|$. In the case of steady shearing flow we find,

$$\left. \begin{aligned} \tau &= \eta_0 \left(1 + \frac{5}{2}\phi\right) \dot{\gamma} + \mu_p \tilde{p} \\ p &= p_{eq} + \tilde{p}, \end{aligned} \right\} \tag{3.4}$$

with the steady-state packing fraction, $\phi = \phi_{eq}$, given by (2.28).

3.1. Dry granular flow

In steady simple shear flow, dry granular materials have been shown to obey the $\mu(I)$ and $\phi(I)$ rheology as given in Jop *et al.* (2006) and Da Cruz *et al.* (2005),

$$\mu(I) = \mu_1 + \frac{\mu_2 - \mu_1}{1 + (I_0/I)}, \quad \text{and} \quad \phi(I) = \phi_m - cI, \tag{3.5a,b}$$

with c some material constant and where $\mu(I)$ is the ratio between the measured shear stress τ and the measured granular pressure \tilde{p} . This behaviour is captured by our model in the limit that $\eta_0 \rightarrow 0$. By the definitions of the inertial numbers in (2.29), if $\eta_0 = 0$, then $I_m = I$. Additionally, for $\eta_0 = 0$, $\mu = \mu_p$, as given in (2.32). Expanding the expression for ϕ_{eq} from (2.28) around $I = 0$ (where existing data have been collected), we find that our model predicts the following steady shear behaviour,

$$\mu = \mu_1 + \frac{\mu_2 - \mu_1}{1 + (b/I)}, \quad \text{and} \quad \phi \approx \phi_m - a\phi_m I + O(I^2), \tag{3.6a,b}$$

which is a reasonable approximation to known fits of the $\mu(I)$, $\phi(I)$ rheology if $a = (c/\phi_m)$ and $b = I_0$.

3.2. Viscous granular mixtures

Boyer *et al.* (2011) experimentally investigate the steady-state rheology of mixtures undergoing steady, quasi-two-dimensional shear flow at low Stokes numbers. The Stokes number of interest in this context is defined in Amarsid *et al.* (2017) as,

$$St = \frac{\rho_s d^2 \dot{\gamma}}{\eta_0} = \frac{I^2}{I_v}. \tag{3.7}$$

In the limit that $St \rightarrow 0$, the mixed inertial number I_m is dominated by the viscous inertial number I_v , such that $I_m = \sqrt{2I_v}$.

Parameter	$\mu(I_v)$	$\mu(I_v, I_m)$
μ_1	0.32	0.2764
μ_2	0.7	0.8797
I_0	0.005	—
ϕ_m	0.585	0.585
a	—	0.7071
b	—	0.1931

TABLE 2. Parameters for model fit to data in figure 5.

Boyer *et al.* (2011) defines the $\mu(I_v)$ and $\phi(I_v)$ viscous granular rheologies as follows,

$$\mu(I_v) = \mu_1 + \frac{\mu_2 - \mu_1}{1 + (I_0/I_v)} + I_v + \frac{5}{2}\phi_m\sqrt{I_v} \quad \text{and} \quad \phi(I_v) = \frac{\phi_m}{1 + \sqrt{I_v}}. \quad (3.8a,b)$$

It can be shown from (2.28), (2.29) and (2.32) that the steady shear response of our mixture is given by,

$$\mu(I_v, I_m) = \mu_1 + \frac{\mu_2 - \mu_1}{1 + (b/\sqrt{2I_v})} + I_v + \frac{5}{2}\phi_m\sqrt{\frac{I_v}{2a^2}}, \quad \text{and} \quad \phi = \frac{\phi_m}{1 + a\sqrt{2I_v}}. \quad (3.9a,b)$$

The expression for the steady-state packing fraction ϕ in (3.9) identically recovers the $\phi(I_v)$ fit from Boyer *et al.* (2011) when $a = (1/\sqrt{2})$. The $\mu(I_v)$ function of Boyer *et al.* (2011) is not reproduced exactly with our model; however, as shown in figure 5, we can fit our form $\mu(I_v, I_m)$ to their data directly. Strong agreement is found between our model fit, the model fit in Boyer *et al.* (2011) and the data collected in that work. The fit parameters for the plot in figure 5 are given in table 2.

3.3. Suspension effective viscosity

Significant work has been done on understanding the behaviour of co-moving suspensions of granular material in fluids. We are particularly interested in the change in effective fluid viscosity of suspensions due to the solid phase volume fraction as reviewed and summarized in Stickel & Powell (2005) with η_r , the relative viscosity,

$$\eta_r = \frac{\tau}{\eta_0\dot{\gamma}}, \quad \lim_{\phi \rightarrow \phi_m} \eta_r = \infty, \quad \lim_{\phi \rightarrow 0} \frac{\eta_r - 1}{\phi} = [\eta]. \quad (3.10a-c)$$

In the dense limit ($\phi \rightarrow \phi_m$), the viscosity of the suspension approaches infinity and in the dilute limit ($\phi \rightarrow 0$), the viscosity of the mixture should vary linearly with $[\eta]$ where $[\eta] = (5/2)$ for hard spheres (Stickel & Powell 2005).

As in § 3.2, we are concerned with the behaviour of our mixture model in the low Stokes limit such that $I_m = \sqrt{2I_v}$. Therefore we find, $\eta_r = 1 + (5/2)\phi + (\mu_p/I_v)$, which by (2.28) and (2.32) is equivalently,

$$\eta_r(\phi) = 1 + \frac{5}{2}\phi \left(\frac{\phi_m}{\phi_m - \phi} \right) + 2 \left(\frac{a\phi}{\phi_m - \phi} \right)^2 \left(\mu_1 + \frac{\mu_2 - \mu_1}{1 + ab\phi/(\phi_m - \phi)} \right). \quad (3.11)$$

It can be shown that this relation achieves both limiting behaviours required of effective viscosity models.

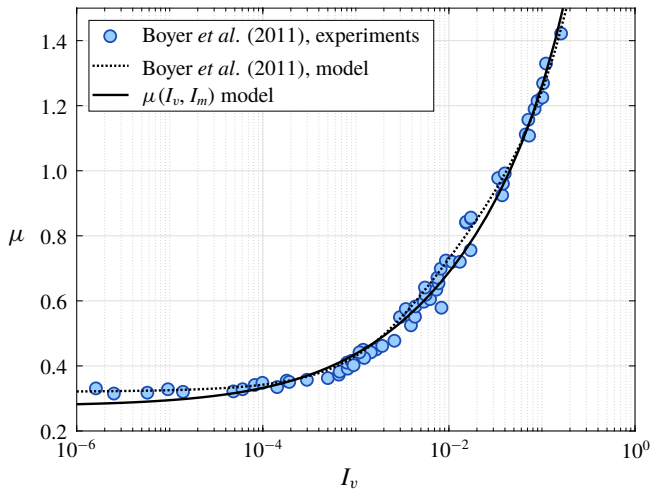


FIGURE 5. (Colour online) Plot of the ratio between the shear stress and effective granular pressure (μ) against the inertial number I_v . Data collected by Boyer *et al.* (2011) are shown as the shaded blue circles. The $\mu(I_v)$ rheology from that work is represented by the dotted line. The combined response of the mixture model presented in this work (see (3.9)) is represented by the solid line.

By noting the similarity of the materials used by Chang & Powell (1994) (polystyrene and poly(methyl methacrylate)), to that used in Boyer *et al.* (2011), we use the coefficients determined in §3.2 and given in table 2 to compare (3.11) against the experimental measurements reported in Chang & Powell (1994) and Boyer *et al.* (2011) (see figure 6).

4. Numerical implementation

We are interested in time-accurate simulations of fluid–sediment mixtures undergoing arbitrarily large deformations. To do this, we use a material point method (MPM) framework capable of simultaneously solving all of the governing equations shown in table 3. This MPM framework is a derivative of that shown in Dunatunga & Kamrin (2015) and borrows heavily from methods described in Abe, Soga & Bandara (2013) and Bandara & Soga (2015).

Figure 7 shows the basic method we implement. First, the mixture problem is defined and the material configurations are given (figure 7*a*). The two phases are then separated into the continuum bodies described in figure 2 (figure 7*b*). These continuum bodies are discretized into continuum ‘chunks’ defined by two sets of Lagrangian material point tracers. These tracers carry the full description of the continuum bodies (e.g. stress, density, velocity) and advect material information through space (figure 7*c*). These two sets of tracers are then placed into a simulation domain which is discretized into a background grid. The background grid is where the equation of motion are solved in the weak form (figure 7*d*).

Time integration of the mixture problem is achieved by using an explicit time-marching algorithm. During each discrete time step, the mixture state (stored on the two sets of material points) is projected to the nodes which define the background Cartesian grid. A finite-element-like step is performed which solves the system of equations in table 3 and updates the nodal representation of the mixture velocities and

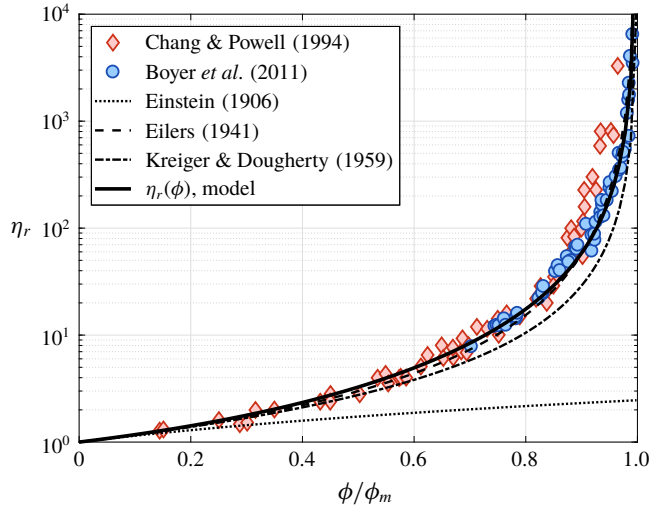


FIGURE 6. (Colour online) Plot of various models for effective viscosity η_r versus the relative packing fraction ϕ/ϕ_m . The model given in this work by (3.11) is shown by the solid line. The red diamonds represent the experimental results reported in Chang & Powell (1994) (from Chong, Christiansen & Baer (1971), Poslinski *et al.* (1988), Storms, Ramarao & Weiland (1990), Shapiro & Probstein (1992), Chang & Powell (1993) and Chang & Powell (1994)). The blue circles represent the experimental results reported in Boyer *et al.* (2011).

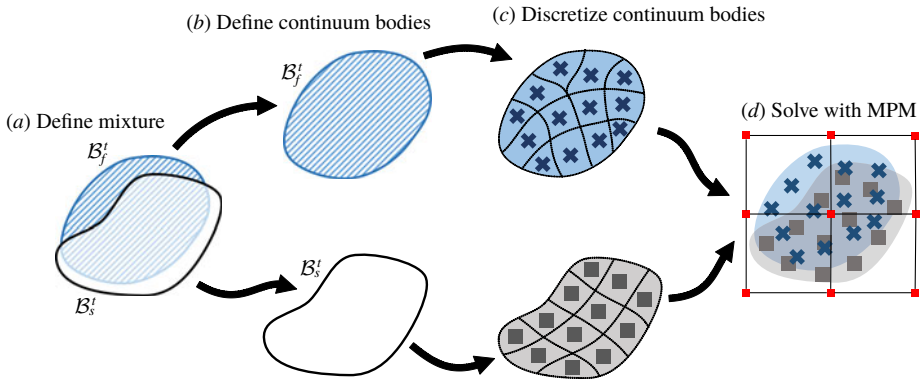


FIGURE 7. (Colour online) Solving mixture problems using the material point method. (a) Define the mixture and initial configuration including densities, porosities, stresses. (b) Define the solid and fluid phase continuum bodies. (c) Break the continuum bodies into piecewise-defined blocks of material represented by discrete material points. (d) Solve the equations of motion for the mixture on a background grid according to the material point method algorithm described in § C.2.

acceleration. These accelerations and velocities are then used to update the mixture state (as stored on the two sets of material points). At the end of the time step, the grid is reset, and the procedure is repeated. In this way, we track the state of the mixture on a moving set of material point tracers and solve the equations of motion

Rule	Expression	Number
Solid phase mass conservation	$\frac{D^s \bar{\rho}_s}{Dt} + \bar{\rho}_s \operatorname{div} \mathbf{v}_s = 0$	(2.5)
Fluid phase mass conservation	$\frac{D^f \bar{\rho}_f}{Dt} + \bar{\rho}_f \operatorname{div} \mathbf{v}_f = 0$	(2.7)
Fluid phase true density	$\frac{n}{\rho_f} \frac{D^f \rho_f}{Dt} = -\operatorname{div} ((1-n)\mathbf{v}_s + n\mathbf{v}_f)$	(2.8)
Solid phase momentum balance	$\bar{\rho}_s \frac{D^s \mathbf{v}_s}{Dt} = \bar{\rho}_s \mathbf{g} - \mathbf{f}_d + \operatorname{div} (\tilde{\boldsymbol{\sigma}}) - (1-n) \operatorname{grad} (p_f)$	(2.13)
Fluid phase momentum balance	$\bar{\rho}_f \frac{D^f \mathbf{v}_f}{Dt} = \bar{\rho}_f \mathbf{g} + \mathbf{f}_d + \operatorname{div} (\boldsymbol{\tau}_f) - n \operatorname{grad} (p_f)$	(2.14)
Darcy’s drag law	$\mathbf{f}_d = \frac{18\phi(1-\phi)\eta_0}{d^2} \hat{F}(\phi, Re) (\mathbf{v}_s - \mathbf{v}_f)$	(2.17)
Fluid phase pore pressure	$p_f = \kappa \ln \left(\frac{\rho_f}{\rho_{of}} \right)$	(2.21)
Fluid phase shear stress	$\boldsymbol{\tau}_f = 2\eta_0 \left(1 + \frac{5}{2}\phi \right) \mathbf{D}_{of}$	(2.23)
Solid phase effective stress	$\frac{D^s \tilde{\boldsymbol{\sigma}}}{Dt} = 2G\mathbf{D}^{e_0} + K \operatorname{tr} (\mathbf{D}^e) \mathbf{1} + \mathbf{W}_s \tilde{\boldsymbol{\sigma}} - \tilde{\boldsymbol{\sigma}} \mathbf{W}_s$	(2.25)
Additive flow rate decomposition	$\mathbf{D}_s = \mathbf{D}^e + \tilde{\mathbf{D}}^p$	(B 7)
Solid phase plastic flow rate	$\tilde{\mathbf{D}}^p = \frac{\dot{\gamma}^p}{\sqrt{2}} \frac{\tilde{\boldsymbol{\sigma}}_0}{\ \tilde{\boldsymbol{\sigma}}_0\ } + \frac{1}{3} (\beta \dot{\gamma}^p + \dot{\xi}_1 + \dot{\xi}_2) \mathbf{1}$	(2.26)
Dilation angle	$\beta = K_3 (\phi - \phi_{eq})$	(2.27)
Critical state packing fraction	$\phi_{eq} = \frac{\phi_m}{1 + aI_m}$	(2.28)
Internal friction coefficient	$\mu_p = \mu_1 + \frac{\mu_2 - \mu_1}{1 + (b/I_m)} + \frac{5}{2} \left(\frac{\phi I_v}{aI_m} \right)$	(2.32)
Granular shear flow rule	$f_1 = \bar{\tau} - \max((\mu_p + \beta)\bar{p}, 0)$ $f_1 \leq 0, \quad \dot{\gamma}^p \geq 0, \quad f_1 \dot{\gamma}^p = 0$	(2.30)
Granular separation rule	$f_2 = -\bar{p}$ $f_2 \leq 0, \quad \dot{\xi}_1 \geq 0, \quad f_2 \dot{\xi}_1 = 0$	(2.33)
Granular compaction rule	$f_3 = g(\phi)\bar{p} - (a\phi)^2 [\zeta^2 d^2 \rho_s + 2\eta_0 \zeta]$ $f_3 \leq 0, \quad \dot{\xi}_2 \leq 0, \quad f_3 \dot{\xi}_2 = 0$ $\zeta = \dot{\gamma}^p - K_4 \dot{\xi}_2$	(2.34)
	$g(\phi) = \begin{cases} (\phi_m - \phi)^2 & \text{if } \phi < \phi_m \\ 0 & \text{if } \phi \geq \phi_m \end{cases}$	(2.35)

TABLE 3. Summary of governing equations derived in §2.

of a background finite-element-like grid. Specific details about our implementation of this framework, boundary conditions and novel numerical corrections can be found in appendix B.

5. Results

To validate our model, we use the numerical method described in §4 to simulate underwater column collapses and quasi-two-dimensional erosion flows for comparison

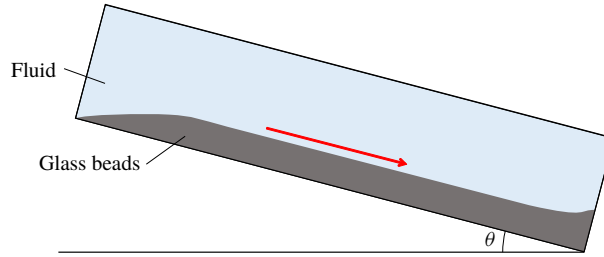


FIGURE 8. (Colour online) Experimental geometry used by Pailha & Pouliquen (2009). A bed of glass beads is immersed in a tank of viscous fluid. The incline of the base of the tank, θ , is changed to induce submerged slope avalanches.

with experimental data reported by Rondon, Pouliquen & Aussillous (2011) and Allen & Kudrolli (2017). We also explore two applications of our method for potential use in impact/penetration problems (as explored in Ceccato *et al.* (2016)) or for loaded slope failures (see summary of numerical work in this area by Soga *et al.* (2015)).

5.1. Numerical validation of model and method

In this section, we show that our model parameters can be fit to a particular class of fluid–sediment mixtures (in this case glass beads immersed in oil/water mixtures, see Pailha & Pouliquen (2009)) and that these fit parameters can be used to accurately simulate an underwater column collapse (from Rondon *et al.* 2011) and quasi-two-dimensional erosion flows (from Allen & Kudrolli 2017).

5.1.1. Model fit to glass beads

Pailha & Pouliquen (2009) characterize the behaviour of glass beads flowing down a chute while immersed in a viscous fluid (set-up shown in figure 8). The glass beads have density $\rho_s = 2500 \text{ kg m}^{-3}$ and diameter $d = 160 \text{ }\mu\text{m}$. Two mixtures of water/oil are reported and have viscosities $\eta_0 = 9.8 \times 10^{-3} \text{ Pa s}$ and $\eta_0 = 96 \times 10^{-3} \text{ Pa s}$.

In order to fit our model to the characterization of this mixture, we have focused on a subset of the reported data shown in figure 9. Figure 9(b) shows the measured packing fraction of numerous flows/times plotted against the inertial number I_b (defined in Pailha & Pouliquen (2009)). We assume that the chute flow profile is parabolic (as is proven in Cassar, Nicolas & Pouliquen (2005)) such that $I_b \approx I_v$. We further assume that all of the reported flows are in the low Stokes limit ($St \rightarrow 0$) such that $I_m \approx \sqrt{2I_b}$. Fitting (2.28) to the lower extrema of the data, we find the following material parameters,

$$\phi_m = 0.584, \quad a = 1.23. \quad (5.1a,b)$$

Figure 9(a) shows the measured internal friction angle $\tan(\theta)$ plotted against the experimental inertial number I_b . Assuming that all measurements were taken when the flows had reached steady state, $\tan(\theta) \approx \mu$ with μ given in (3.9). Fitting this equation to the data, we find the following material parameters,

$$\mu_1 = 0.35, \quad \mu_2 = 1.387, \quad b = 0.3085. \quad (5.2a-c)$$

Figure 9(c) shows a set of flow onset measurements. At the transition from the ‘No flow’ state to the ‘Flow’ state, $\tan(\theta) \approx \mu_1 + \beta$. We assume that near the onset of flow

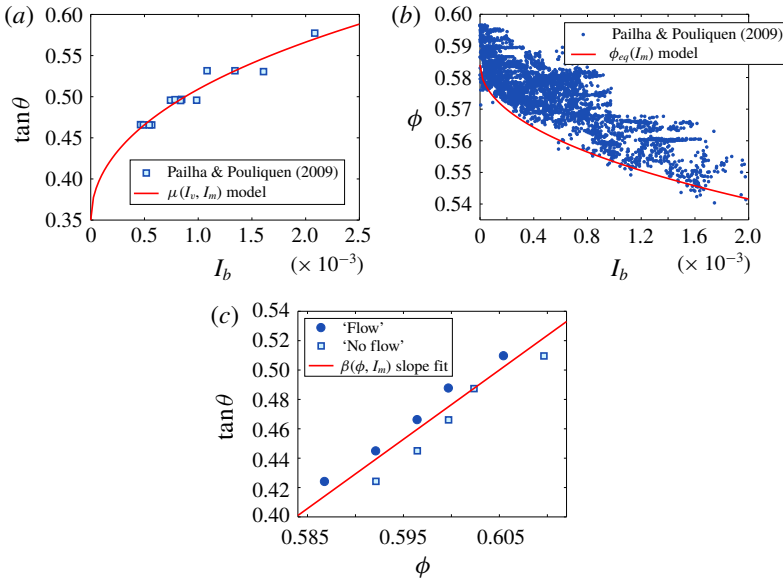


FIGURE 9. (Colour online) Model fit to the experimental data presented in figure 5 of Pailha & Pouliquen (2009). (a) Plot of internal friction coefficient against inertial number. (b) Critical state packing fraction fit to extreme measurements of ϕ at various flow rates. (c) β slope coefficient K_3 and K_4 fit to the critical angle between flowing and static slopes.

$I_m = 0$. Therefore, the slope of the transition line between flowing and non-flowing behaviour will be given by K_3 , and since the rate of compaction in these flows is small (the K_4 term), we let,

$$K_3 = 4.715, \quad K_4 = 0. \tag{5.3a,b}$$

With the parameters above determined for glass beads, we can now simulate other experiments which use similar mixtures. The remaining parameters (ρ_s , ρ_{of} , η_0 and d) are determined by the specific materials used in the relevant experiments.

5.1.2. Granular column collapse of glass beads

Rondon *et al.* (2011) explore the behaviour of collapsing granular columns submerged in a fluid with viscosity $\eta_0 = 12$ or 23 cP and density $\rho_{of} \approx 1000 \text{ kg m}^{-3}$. A bed of glass beads with diameter $d = 225 \text{ }\mu\text{m}$ and density $\rho_s = 2500 \text{ kg m}^{-3}$ was held at some initial packing fraction behind a retaining wall (see figure 10). Once the wall was removed, the dynamics of the column was measured and reported.

In this work, we are interested in the behaviour of two of the columns reported in that work. The two columns are made of the same mass of glass beads and formed into a loose column and a dense column. The loose column has initial height $h_0 = 4.8 \text{ cm}$, initial width $l_0 = 6.0 \text{ cm}$ and initial packing fraction $\phi_0 = 0.55$. The dense column has initial height $h_0 = 4.2 \text{ cm}$, initial width $l_0 = 6.0 \text{ cm}$, and initial packing fraction $\phi_0 = 0.60$. Both columns are immersed in a fluid tank measuring $70 \text{ cm} \times 15 \text{ cm} \times 15 \text{ cm}$. It was observed that the initially loose column collapsed much faster with much longer run-out than the initially dense column.

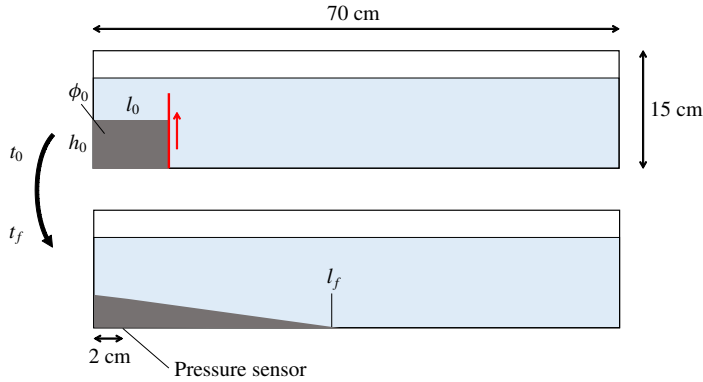


FIGURE 10. (Colour online) The experimental set-up used by Rondon *et al.* (2011). A column of small glass spheres with initial packing fraction ϕ_0 is held in place by a retaining wall and immersed in a long tank filled with a viscous fluid. At time t_0 , the wall is removed and the column is allowed to collapse. A pressure sensor at the base of the column (2 cm from the edge of the tank) collects pore pressure data during the collapse. The run-out profiles of the column are captured with a camera.

Parameter	300×100 Simulations	120×40 Simulations
Elements	300×100	120×40
Points per cell	4	4
Δt	5×10^{-5} s	2×10^{-5} s
Δx	1.0 mm	2.5 mm
t_0	0 s	0 s
t_f	20 s	60 s
G	3.8×10^4 Pa	3.8×10^5 Pa
K	8.3×10^4 Pa	8.3×10^5 Pa
η_0	1.2×10^{-2} Pa s	1.2×10^{-2} Pa s
κ	1.0×10^5 Pa	1.0×10^6 Pa

TABLE 4. Simulation parameters for column collapses run on different grids.

To simulate these two column collapses, we consider a reduced computational domain by assuming that the flow is approximately plane strain (quasi-two-dimensional) and that the fluid tank can be shortened to 30 cm in length and 10 cm in height without significantly affecting the dynamics of the column collapse (we let the fluid partially fill the tank to a height of 8 cm). We then run our model with the same initial conditions as described in Rondon *et al.* (2011), computational parameters given in table 4 and remaining material parameters given in §5.1.1. The fluid–wall interaction is governed by a simple frictionless boundary condition while the grain–wall interaction is governed by the frictional boundary rule described in §C.4.2.

In both the experiments and simulations, the only differences between the dense and loose columns are the initial packing fraction, the initial column height and the initial hydrostatic stress state. The resulting differences in the simulated flow dynamics are due to the different solutions picked out by the governing equations given these initial conditions. A series of snapshots taken from these two simulations (as run on

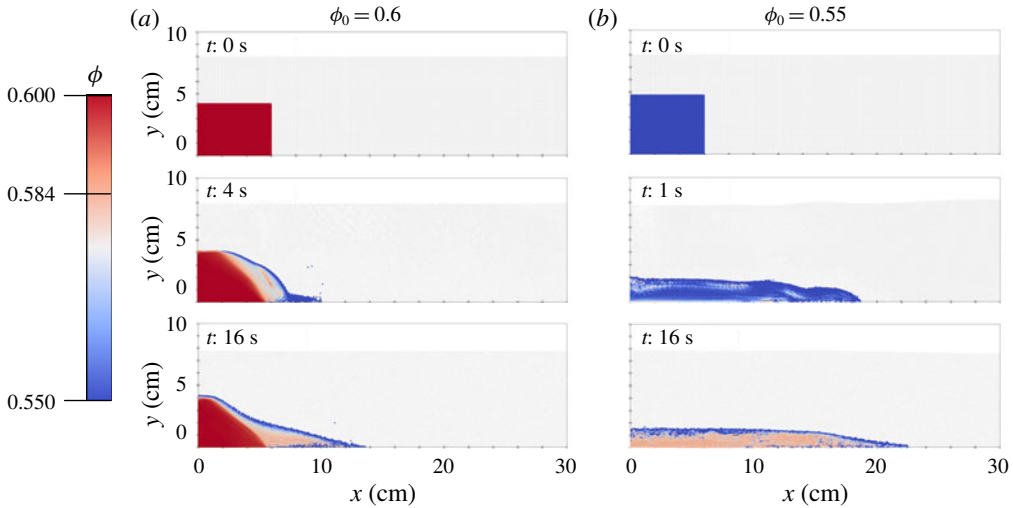


FIGURE 11. (Colour online) Comparison between simulated collapses for the loose initial packing (b) and the dense initial packing (a) using the 300×100 element grid described in table 4. Solid phase material points are coloured by packing fraction according to the scale at the left. Fluid phase material points are coloured light grey.

the 300×100 grid) are shown in figure 11; see supplementary movie 1 (available at <https://doi.org/10.1017/jfm.2018.914>) of these simulations.

In addition to visualizing the solid phase dilation and compaction as in figure 11, we can also examine the differences in shearing rate and fluid pore pressure as shown in figure 12. As the initially dense column collapses, the solid phase experiences shear dilation, increasing the porosity of the mixture. This results in pore tension in the fluid phase as fluid is drawn into the increased pore space (see figure 12a). This increased pore tension within the collapsing column (as compared to the surrounding fluid) increases the effective granular pressure given by \tilde{p} in (2.31) and therefore strengthens the solid phase resulting in a slower collapse process. On the other hand, as the initially loose column collapses the solid phase experiences plastic compaction, reducing the porosity of the mixture. This has the opposite effect, causing an excess positive pore pressure (see figure 12b) which reduces the strength of the solid phase. It is this coupling of solid phase flow to fluid phase pressure to solid phase strength that results in these two completely different collapse behaviours.

By accurately modelling these complex interactions, we are able to capture the vastly different collapse profiles (see figure 13), predict the measured excess pore pressure (see figure 14a) and match the time-accurate front motion (see figure 14b) reported in Rondon *et al.* (2011). The collapse profiles shown in figure 13 are the $n = 0.45$ contours of the nodal porosity field $n(x)$ and show reasonable similarity to the experimental profiles, although there are some artefacts of the finite grid spacing visible near the front of the collapsing column.

The pore pressure in figure 14(b) shows the weighted average nodal representation of pressure (as defined in Dunatunga & Kamrin (2015)) near (but not at) the lower domain boundary and 2 cm from the left wall. This value is compared to a hydrostatic reference value to find the excess pore pressure. In the dense 300×100 simulation, the fluid phase material points exhibited excessive clumping (see § C.4.5), so a second nodal sample was taken at the same height, 2 cm from the right wall and used as the

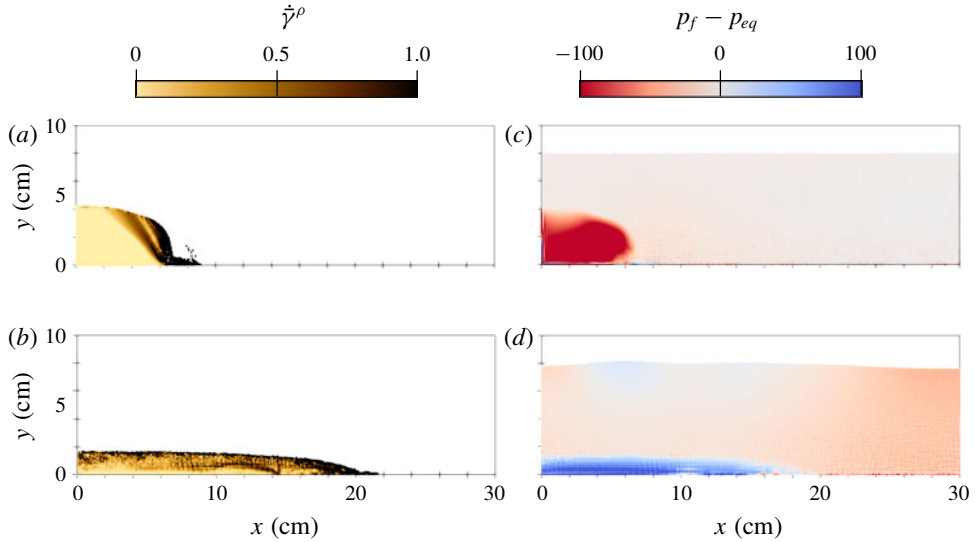


FIGURE 12. (Colour online) Snapshot of simulated solid phase equivalent plastic shear rate (a,b) and fluid phase excess pore pressure (c,d) at $t=4$ s for (a,c) the initially dense column and (b,d) the initially loose column. The plastic shearing rate is visualized at the material point centroids of the solid phase. The post-processed excess pore pressure (see Dunatunga & Kamrin (2015)) as compared to a hydrostatic baseline p_{eq} is visualized at the fluid phase centroids.

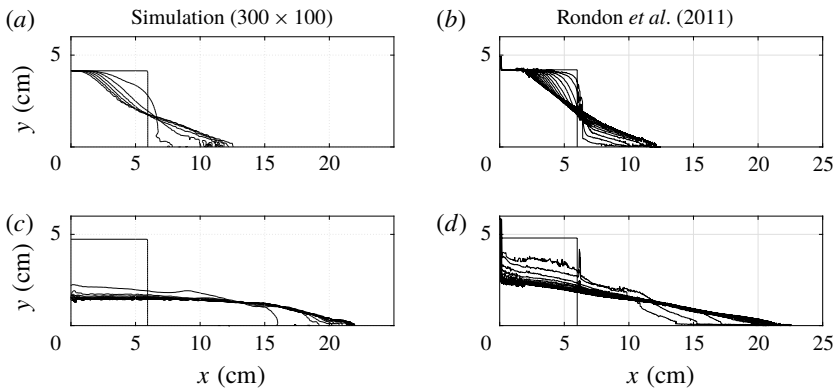


FIGURE 13. Contours of the collapsing columns from the dense simulation (a) taken at 3 s intervals and the loose simulation (c) taken at 0.66 s intervals. The corresponding contours for the dense experiment (b) and loose experiment (d) from Rondon *et al.* (2011) are also shown. The simulated profiles are generated by plotting the contour of the nodal porosity field (given by the coefficients $\{n_i\}$) at $n=0.45$.

reference value. The front positions shown in figure 14(b) are determined by taking the maximum x -position of the collapse profiles shown in figure 13.

The time history of the simulated pore pressures in figure 14 show close agreement to the experimental measurements; however, the dense simulations appear to saturate at a negative excess pore pressure. This discrepancy is likely due to the high frequency

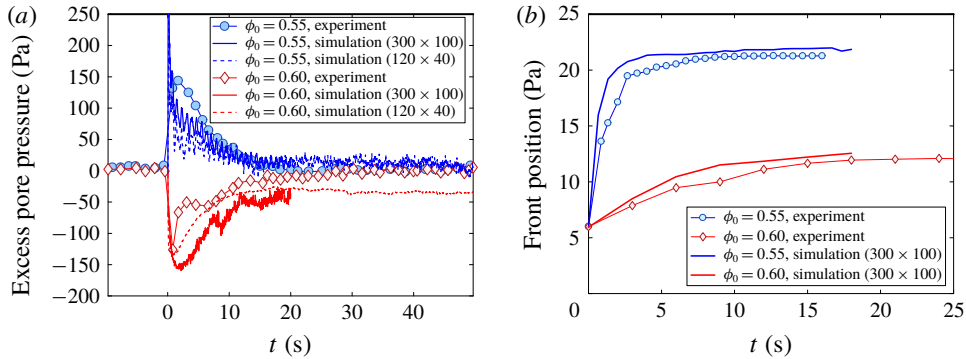


FIGURE 14. (Colour online) (a) Comparison of the simulated excess pore pressure for the loose initial packing (top, blue) and the dense initial packing (bottom, red). The base pore pressure for all simulations is approximately 800 Pa. (b) Comparison between simulated front positions for the loose initial packing (top, blue) and the dense initial packing (bottom, red).

error observed in the MPM stress field before nodal averaging (see Dunatunga & Kamrin (2015)). Mast *et al.* (2012) propose several methods of mitigating these errors and the associated kinematic locking, but we do not implement them here. Altogether, the results shown in figures 13 and 14 indicate that our model is capable of accurately predicting the dynamics of submerged granular column collapses and captures the sensitivity of the problem to small changes in initial conditions.

5.1.3. Quasi-two-dimensional flow of glass beads

In addition to sudden collapses of granular columns, we are also interested in using our model to simulate steady erosion processes. To gage the accuracy of our method for such problems, we simulate the experiments performed by Allen & Kudrolli (2017). As shown in figure 15, the experimental set-up, approximates a two-dimensional (2-D) erosion flow by driving a conical motor at a prescribed rotation rate, f , above an immersed granular bed of glass beads. The fields reported, obtained using index-matching, are a function of vertical depth below the driving surface, z .

The mixture of fluid and grains used in Allen & Kudrolli (2017) is similar to that used in Pailha & Pouliquen (2009), suggesting that we can use the same material parameters determined in § 5.1.1. The remaining material parameters are given by the specific materials used in the experiment: $\rho_{of} = 1002 \text{ kg m}^{-3}$, $\eta_0 = 0.021 \text{ Pa s}$, $\rho_s = 2500 \text{ kg m}^{-3}$ and $d = 1.05 \text{ mm}$.

We simulate four of the reported flows in that work, $f/f_c = \{0.37, 1.04, 1.26, 1.33\}$, where f is the assigned driving frequency and f_c is the reported critical driving frequency around which grains become suspended in the fluid flow. We set up an x -periodic domain measuring $15.5 \text{ mm} \times 15.5 \text{ mm}$ and drive the upper surface at a velocity determined by the ratios the driving frequency f . We let the lower wall be governed by a no-slip boundary condition. The resulting fluid flow is allowed to reach steady state and the flow properties are averaged over a 12 s time window. A summary of the simulation set-up is given in table 5.

A series of simulation snapshots is shown in figure 16; see supplementary movie 2 to view a video of these simulations. As was observed in Allen & Kudrolli (2017),

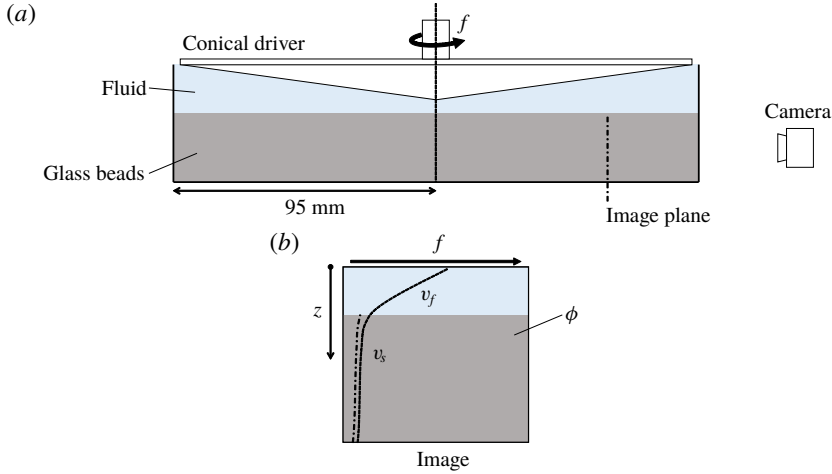


FIGURE 15. (Colour online) (a) Experimental set-up of Allen & Kudrolli (2017). An approximately 9 mm bed of grains is immersed in a cylindrical tank filled with fluid. A conical driver is submerged to the granular surface and driven by a motor at a specified rotation rate f . (b) The resulting flow is imaged at a plane near the edge of the tank. Measurements are taken of phase velocities and packing fractions as a function of distance z from the driving surface.

Parameter	$f/f_c = 0.37$	$f/f_c = 1.04$	$f/f_c = 1.26$	$f/f_c = 1.33$
Bed height	10.5 mm	11.0 mm	11.0 mm	11.4 mm
Driving velocity	0.2325 m s^{-1}	0.6536 m s^{-1}	0.7919 m s^{-1}	0.8359 m s^{-1}
Elements	20×20	20×20	20×20	20×20
Points per cell	9	9	9	9
Δt	$2 \times 10^{-5} \text{ s}$	$2 \times 10^{-5} \text{ s}$	$2 \times 10^{-5} \text{ s}$	$2 \times 10^{-5} \text{ s}$
Δx	775 μm	775 μm	775 μm	775 μm
t_0	0 s	0 s	0 s	0 s
t_f	30 s	30 s	30 s	30 s
G	$3.8 \times 10^4 \text{ Pa}$	$3.8 \times 10^4 \text{ Pa}$	$3.8 \times 10^4 \text{ Pa}$	$3.8 \times 10^4 \text{ Pa}$
K	$8.3 \times 10^4 \text{ Pa}$	$8.3 \times 10^4 \text{ Pa}$	$8.3 \times 10^4 \text{ Pa}$	$8.3 \times 10^4 \text{ Pa}$
η_0	$2.1 \times 10^{-2} \text{ Pa s}$	$2.1 \times 10^{-2} \text{ Pa s}$	$2.1 \times 10^{-2} \text{ Pa s}$	$2.1 \times 10^{-2} \text{ Pa s}$
κ	$1.0 \times 10^5 \text{ Pa}$	$1.0 \times 10^5 \text{ Pa}$	$1.0 \times 10^5 \text{ Pa}$	$1.0 \times 10^5 \text{ Pa}$
ϕ_0	0.585	0.585	0.585	0.585

TABLE 5. Simulation parameters for four erosion flows run at different driving velocities.

below the critical driving frequency f_c there is essentially no flow of grains; however, once the driving frequency f is increased above f_c , solid phase material is ‘picked up’ by the shearing of the fluid phase and enters into suspension. The steady-state flow predicted by our simulations shows strong similarity to the experimentally measured packing fraction (see figure 17) and phase velocities (see figure 18).

The simulated packing fractions and velocities are plotted by averaging the material point coefficients over a 12 s window. The resulting phase velocity and packing fraction averages are then sorted by the average material point centroid position and filtered using the MATLAB `smooth()` function. It is important to note that as the solid phase dilates, the solid phase material points will separate. After the material

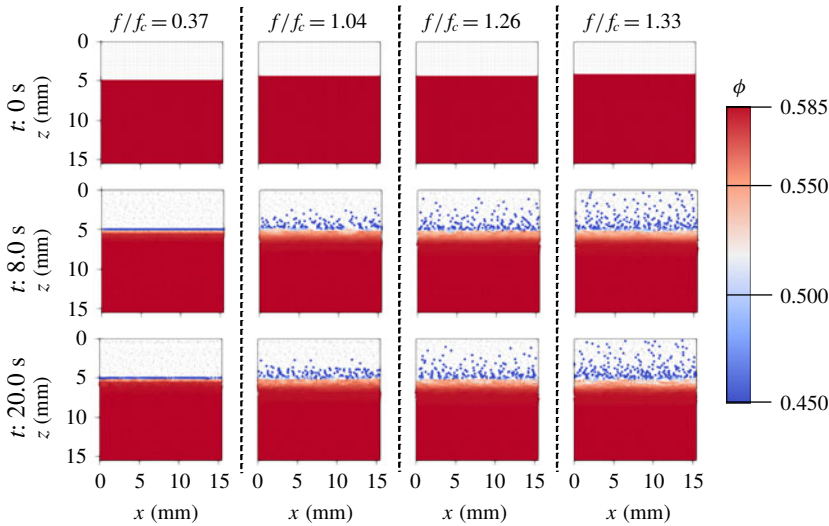


FIGURE 16. (Colour online) Comparison between the simulated erosion flows described in table 5. Solid phase material points are coloured by packing fraction according to the scale at the right. Fluid phase material points are coloured light grey. In all cases, the shearing of the fluid phase induces motion in the solid phase. As the driving frequency f increases above the critical f_c (as reported in Allen & Kudrolli (2017)) solid phase material is ‘picked up’ and becomes suspended in the fluid.

points separate by more than 1 element (around $\phi \approx 0.2$), the material point value ϕ_p will no longer be representative of the true mixture packing fraction.

5.2. Qualitative results

In this section we consider two potential applications of our model and method. The first shows the behaviour of a fluid–grain mixture as an intruding body is pressed into its surface. The second shows the effect of water level on the failure of a loaded slope.

5.2.1. Two-dimensional circular intruder

The use of the material point method for intrusion into a saturated soil is explored at length in Ceccato *et al.* (2016). In that work, the mixture model developed in Bandara & Soga (2015) is adjusted to use the Modified Cam Clay model to model the solid phase behaviour.

Here we show that our model may be extended to explore similar problems by simulating the intrusion of a disk into a submerged bed of acrylic beads. As an exploratory problem, we use the material parameters given in table 2 and let $d = 1.0$ cm, $\rho_s = 2500$ kg m⁻³ and $\rho_f = 1000$ kg m⁻³. A 1 m × 1 m domain is simulated on a 100 × 100 element grid with four material points per cell. The domain is initially half-filled by a mixture of fluid and grains with packing fraction $\phi_0 = 0.60$. The resulting behaviour is shown in figure 19; see supplementary materials for a movie of this simulation. As the intruder enters the mixture, we observe shear dilation of the granular material and independent motion of the two phases of material as fluid fills in the opening pore space under the intruder, revealing dry granular media at the free surface.

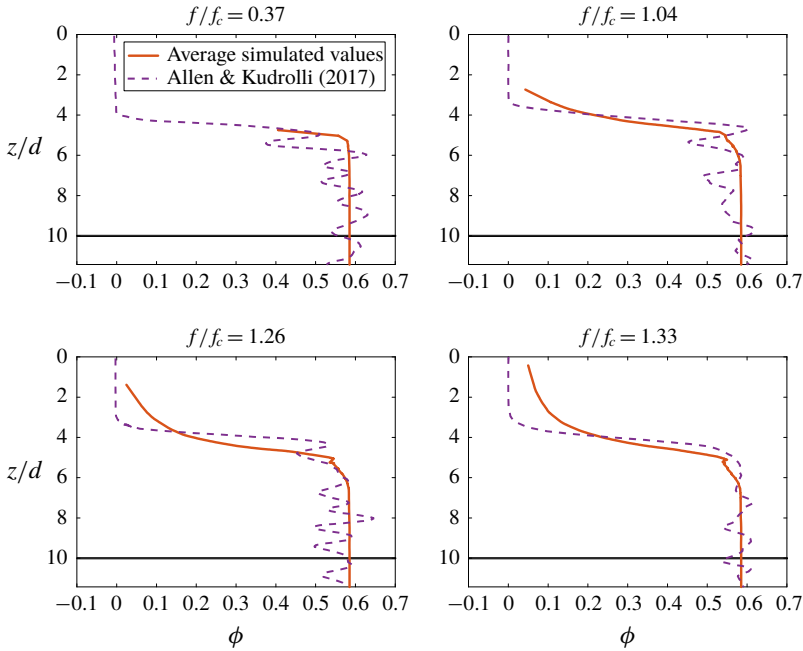


FIGURE 17. (Colour online) Plots comparing the time-averaged steady-state packing fractions as a function of normalized depth reported in Allen & Kudrolli (2017) to those found by running the simulations described in table 5. Very close matching is observed when the solid phase material is dense; however the simulated data have a heavy tail in the dilute regime. This is likely due to the large empty spaces between the solid phase material points when they become suspended in the fluid flow.

5.2.2. Two-dimensional slope collapse

Another application of interest for our model is the complex interactions between structures and saturated soils. To demonstrate the application of this model to the problem of a loaded slope, we consider two simple cases. In the first case, a dry slope with length 14 m and height 5 m is loaded with a cement block at the top (see figure 20). The slope is composed of 2 mm diameter grains with density $\rho_s = 2500 \text{ kg m}^{-3}$. In the second case, an identical slope with identical loading and material composition is partially submerged in water (approximating a shoreline).

The simulations are performed in a $40 \text{ m} \times 10 \text{ m}$ domain discretized into 160×40 elements. The material points for the three bodies are seeded with nine material points per grid cell. The initial packing of the granular slope is $\phi_0 = 0.585$. The resulting collapses are shown in figure 20; see supplemental Movie4 to view a movie of these simulations. We let the material properties be identical to those given in § 5.1.1. As shown in figure 21, the resulting motion of the block (approximating a structure) on top of the slope has a strong dependence on the water level in the slope. Over the course of 5 simulated seconds, the block on the partially submerged slope moves 20% more in the x -direction, 36% more in the y -direction and rotates 34% less.

6. Conclusion

We have developed a full set of constitutive relations for fluid–sediment mixtures which is capable of accurately and robustly modelling both dense and dilute flows

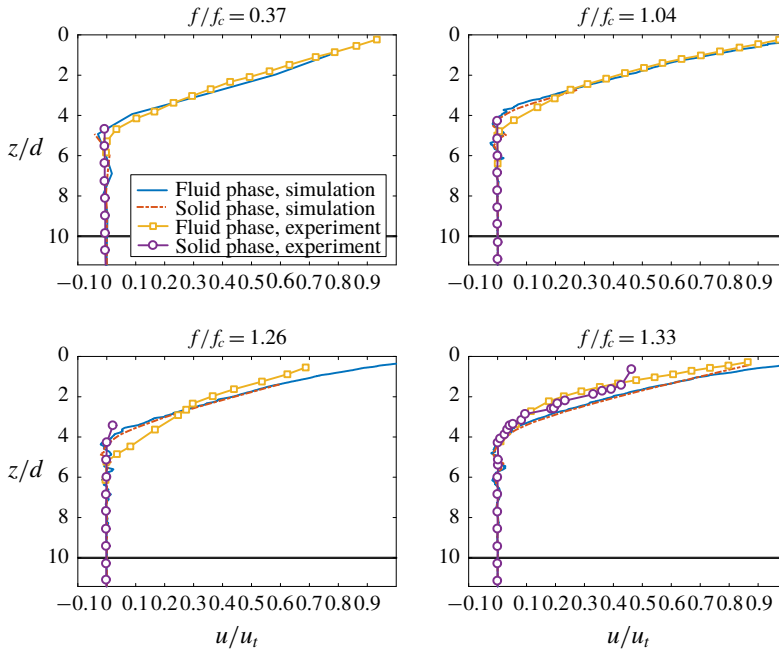


FIGURE 18. (Colour online) Plots comparing the time-averaged steady-state phase velocities u (normalized by the velocity of the driving surface u_t) as a function of normalized depth reported in Allen & Kudrolli (2017) to those found by running the simulations described in table 5. The simulated values show strong similarity to the experimental values; however, there are oscillations visible in the simulated profiles. These oscillations are due to well-known errors in the material point velocity fields.

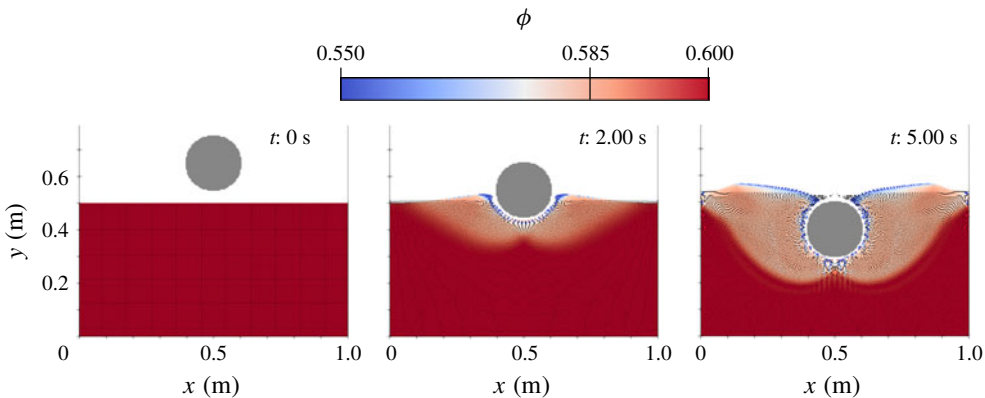


FIGURE 19. (Colour online) Series of snapshots taken from simulation described in § 5.2.1. Solid phase material points are coloured according to packing fraction. Fluid material points are represented by small black dots. Intruder material points are coloured light grey. As the intruder enters the mixture, the shearing of the solid phase results in noticeable dilation.

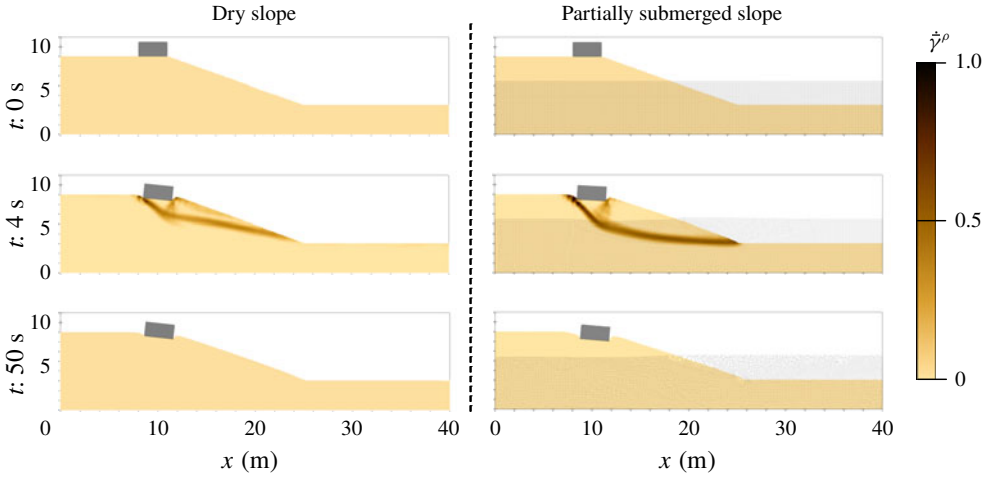


FIGURE 20. (Colour online) Series of snapshots taken from simulations described in § 5.2.2. Solid phase material points are coloured according to the equivalent plastic shearing rate, $\dot{\gamma}^p$. Fluid material points are represented by light grey dots. Block material points are coloured light grey.

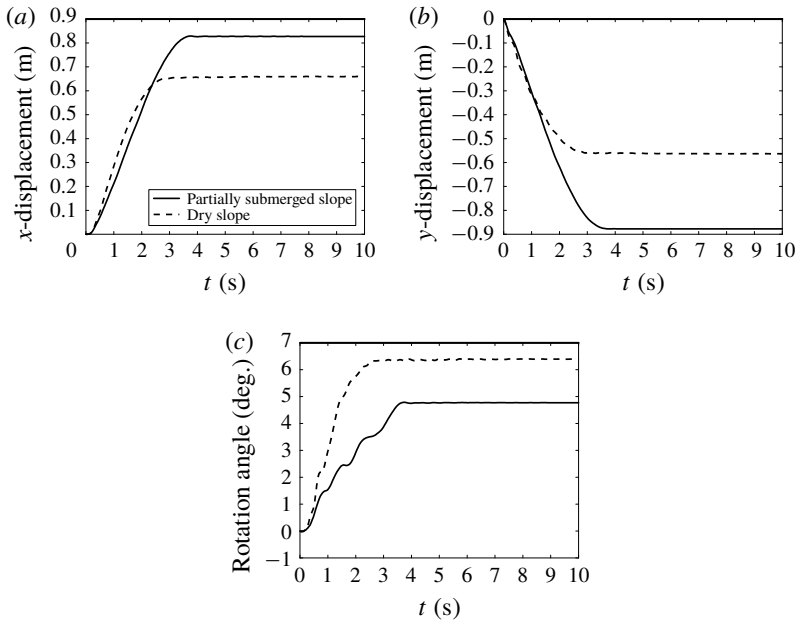


FIGURE 21. Plots of block motion for simulations described in § 5.2.2. (a) The x -displacement of the block's centre of mass. (b) The y -displacement of the block's centre of mass. (c) The rotation of the block about its centre of mass.

of material. Our model is derived from a thermodynamically consistent set of rules and formulated to capture the dry and viscous inertial rheologies of granular materials, the critical state behaviour of grains under shear, the change in the effective viscosity of the fluid due to suspended sediments and a robust Darcy-like inter-phase drag.

This model is implemented in MPM and validated against experiment. We characterize mixtures of glass beads immersed in a Newtonian fluid by fitting our model to the experimental data reported in Pailha & Pouliquen (2009). We then take these material parameters and show that our model is able to accurately predict the behaviour of both collapsing granular columns (see Rondon *et al.* 2011) and shearing of fluid above granular beds (see Allen & Kudrolli 2017) without re-fitting material properties. In addition, we also look at the application of this model and method to the problems of intrusion and slope stability.

The model we have presented in this work may be extensible to more general fluid–sediment mixtures such as those involving air (especially for examining the kick-up of dust for vertical take-off and landing vehicles). Other extensions of this model may look at adding cohesion (redefining the f_1 and f_2 yield conditions), introducing a fabric tensor to the rules governing dilation or adding non-local effects (Kamrin & Koval 2012; Henann & Kamrin 2013; Kamrin & Henann 2015) to capture, for example, the exponential-type decay of the granular velocity field deep in fluid-driven beds (Houssais *et al.* 2015; Allen & Kudrolli 2017).

Acknowledgements

This work was supported by Army Research Office grant W911NF-16-1-0440 and National Science Foundation grant CBET-1253228. We thank P. Aussilous for access to experimental data from Rondon *et al.* (2011).

Supplementary movies

Supplementary movies are available at <https://doi.org/10.1017/jfm.2018.914>.

Appendix A

The constitutive rules for our material model given in table 1 are derived in the following specialization of the two-phase thermodynamic analysis from Drumheller (2000). The basic rules for our model are similar to those described in Coussy (2004); however, our derivation allows for two mixture temperatures, ϑ_s and ϑ_f , and (as mentioned previously) we do not explicitly account for tortuosity.

A.1. First law of thermodynamics

The first law of thermodynamics states that the rate of change of the total energy stored within a volume must be equal to the rate of heat flow into the volume plus the external power exerted on the volume. The total energy stored within a volume is the sum of internal energy and kinetic energy. We define a local expression for the energy conservation in the mixture in terms of the specific internal energies ε_s and ε_f , the phase-wise external heat fluxes \mathbf{q}_s and \mathbf{q}_f , the phase-wise internal heat generation q_s and q_f and the basic homogenized continuum fields from § 2.1.1,

$$\begin{aligned} & \bar{\rho}_s \frac{D^s \varepsilon_s}{Dt} + \bar{\rho}_f \frac{D^f \varepsilon_f}{Dt} + \bar{\rho}_s \frac{D^s \mathbf{v}_s}{Dt} \cdot \mathbf{v}_s + \bar{\rho}_f \frac{D^f \mathbf{v}_f}{Dt} \cdot \mathbf{v}_f \\ & = (\text{div}(\boldsymbol{\sigma}_s) + \bar{\rho}_s \mathbf{g}) \cdot \mathbf{v}_s + (\text{div}(\boldsymbol{\sigma}_f) + \bar{\rho}_f \mathbf{g}) \cdot \mathbf{v}_f \\ & \quad + \boldsymbol{\sigma}_s : \text{grad}(\mathbf{v}_s) + \boldsymbol{\sigma}_f : \text{grad}(\mathbf{v}_f) \\ & \quad + q_s + q_f - \text{div}(\mathbf{q}_s + \mathbf{q}_f) \end{aligned} \tag{A 1}$$

which, with the momentum balance expressions in (2.9), the buoyant force from (2.10), the specific form of the phase stresses in (2.11) and (2.12) and the evolution law for

the true fluid density from (2.8), becomes,

$$\begin{aligned} \bar{\rho}_s \frac{D^s \varepsilon_s}{Dt} + \bar{\rho}_f \frac{D^f \varepsilon_f}{Dt} &= p_f \left(\frac{n}{\rho_f} \frac{D^f \rho_f}{Dt} \right) + \mathbf{f}_d \cdot (\mathbf{v}_s - \mathbf{v}_f) \\ &+ \tilde{\boldsymbol{\sigma}} : \text{grad}(\mathbf{v}_s) + \boldsymbol{\tau}_f : \text{grad}(\mathbf{v}_f) \\ &+ q_s + q_f - \text{div}(\mathbf{q}_s + \mathbf{q}_f). \end{aligned} \tag{A2}$$

A.2. Second law of thermodynamics

The second law of thermodynamics states that the rate of change of the total entropy within a volume Ω must always be greater than or equal to the combined entropy flow into the volume. Drumheller (2000) gives the following necessary condition for entropy imbalance of a mixture,

$$\bar{\rho}_s \frac{D^s s_s}{Dt} + \bar{\rho}_f \frac{D^f s_f}{Dt} + \text{div} \left(\frac{\mathbf{q}_s}{\vartheta_s} + \frac{\mathbf{q}_f}{\vartheta_f} \right) - \frac{q_s}{\vartheta_s} - \frac{q_f}{\vartheta_f} \geq 0. \tag{A3}$$

We add two additional conditions by considering the entropy flow into each phase separately including the entropy flow due to the inter-phase heat flow q_i ,

$$\left. \begin{aligned} \bar{\rho}_s \frac{D^s s_s}{Dt} + \text{div} \left(\frac{\mathbf{q}_s}{\vartheta_s} \right) - \frac{q_s - q_i}{\vartheta_s} &\geq 0 \\ \bar{\rho}_f \frac{D^f s_f}{Dt} + \text{div} \left(\frac{\mathbf{q}_f}{\vartheta_f} \right) - \frac{q_f + q_i}{\vartheta_f} &\geq 0. \end{aligned} \right\} \tag{A4}$$

In the absence of inter-phase heat flow, satisfying the conditions in (A4) also necessarily satisfies (A3). Combining these last two expressions we find a second condition for entropy balance which does not depend on the inter-phase heat flow, q_i .

$$\bar{\rho}_s \vartheta_s \frac{D^s s_s}{Dt} + \bar{\rho}_f \vartheta_f \frac{D^f s_f}{Dt} - \left(\frac{\mathbf{q}_s \cdot \text{grad}(\vartheta_s)}{\vartheta_s} + \frac{\mathbf{q}_f \cdot \text{grad}(\vartheta_f)}{\vartheta_f} \right) + \text{div}(\mathbf{q}_s + \mathbf{q}_f) - (q_s + q_f) \geq 0. \tag{A5}$$

A.3. Helmholtz free energy

We now introduce the definition for the phase-wise Helmholtz free energies, ψ_s and ψ_f , such that,

$$\left. \begin{aligned} \psi_s &= \varepsilon_s - s_s \vartheta_s \\ \psi_f &= \varepsilon_f - s_f \vartheta_f. \end{aligned} \right\} \tag{A6}$$

Substituting into the first law expression in (A2) and combining with the second law expression from (A5), the following free energy inequality is found,

$$\begin{aligned} 0 \leq & -\bar{\rho}_s \frac{D^s \psi_s}{Dt} - \bar{\rho}_f \frac{D^f \psi_f}{Dt} - \bar{\rho}_s s_s \frac{D^s \vartheta_s}{Dt} - \bar{\rho}_f s_f \frac{D^f \vartheta_f}{Dt} \\ & + p_f \left(\frac{n}{\rho_f} \frac{D^f \rho_f}{Dt} \right) + \mathbf{f}_d \cdot (\mathbf{v}_s - \mathbf{v}_f) + \tilde{\boldsymbol{\sigma}} : \text{grad}(\mathbf{v}_s) \\ & + \boldsymbol{\tau}_f : \text{grad}(\mathbf{v}_f) - \frac{\mathbf{q}_s \cdot \text{grad}(\vartheta_s)}{\vartheta_s} - \frac{\mathbf{q}_f \cdot \text{grad}(\vartheta_f)}{\vartheta_f}. \end{aligned} \tag{A7}$$

We let the spatial solid phase and fluid phase velocity gradients be expressed in matrix form as,

$$\mathbf{L}_s \equiv \text{grad}(\mathbf{v}_s), \quad \mathbf{L}_f \equiv \text{grad}(\mathbf{v}_f), \tag{A 8a,b}$$

which have unique decompositions into a phase spin tensor, \mathbf{W} , and a phase strain-rate tensor, \mathbf{D} ,

$$\mathbf{D} = \text{sym}(\mathbf{L}) = \frac{1}{2}(\mathbf{L} + \mathbf{L}^\top), \quad \text{and} \quad \mathbf{W} = \text{skw}(\mathbf{L}) = \frac{1}{2}(\mathbf{L} - \mathbf{L}^\top). \tag{A 9a,b}$$

We further assume that the solid and fluid phases have uniform and constant temperatures, ϑ_s and ϑ_f , such that (A 7) becomes,

$$-\bar{\rho}_s \frac{D^s \psi_s}{Dt} - \bar{\rho}_f \frac{D^f \psi_f}{Dt} + p_f \left(\frac{n}{\rho_f} \frac{D^f \rho_f}{Dt} \right) + (\tilde{\boldsymbol{\sigma}} : \mathbf{D}_s) + (\boldsymbol{\tau}_f : \mathbf{D}_{of}) + \mathbf{f}_d \cdot (\mathbf{v}_s - \mathbf{v}_f) \geq 0. \tag{A 10}$$

A.4. Fluid phase free energy function

The conservative constitutive behaviour of the fluid phase is governed by the fluid phase specific free energy, ψ_f . We assume that the functional form of the free energy only depends on the true fluid density, $\psi_f = \hat{\psi}_f(\rho_f)$. Substituting into the expression for free energy imbalance in (A 10),

$$-\bar{\rho}_s \frac{D^s \psi_s}{Dt} + (\tilde{\boldsymbol{\sigma}} : \mathbf{D}_s) - \frac{n}{\rho_f} \frac{D^f \rho_f}{Dt} \left(p_f - \rho_f^2 \frac{\partial \hat{\psi}_f(\rho_f)}{\partial \rho_f} \right) + (\boldsymbol{\tau}_f : \mathbf{D}_{of}) + \mathbf{f}_d \cdot (\mathbf{v}_s - \mathbf{v}_f) \geq 0. \tag{A 11}$$

A.5. Solid phase free energy function

The solid phase behaviour will be governed by an elastic–plastic constitutive relation derived from that given in Anand & Su (2005). We begin with the definition of the solid phase deformation gradient,

$$\mathbf{F} = \frac{\partial \boldsymbol{\chi}_s(\mathbf{X}, t)}{\partial \mathbf{X}}, \quad \frac{D^s \mathbf{F}}{Dt} = \mathbf{L}_s \mathbf{F}, \tag{A 12a,b}$$

where $\boldsymbol{\chi}_s(\mathbf{X}, t)$ is the motion function mapping from a position, \mathbf{X} , in the solid reference configuration to a position in the solid deformed (current) configuration at time t .

We assume the Kroner–Lee decomposition of the deformation gradient,

$$\mathbf{F} = \mathbf{F}^e \mathbf{F}^p, \tag{A 13}$$

with \mathbf{F}^e the elastic deformation and \mathbf{F}^p the plastic deformation. With this, the velocity gradient can be separated into an elastic and plastic flow,

$$\mathbf{L}_s = \mathbf{L}^e + \mathbf{F}^e \mathbf{L}^p \mathbf{F}^{e-1}, \quad \text{such that} \quad \frac{D^s \mathbf{F}^e}{Dt} = \mathbf{L}^e \mathbf{F}^e, \quad \frac{D^s \mathbf{F}^p}{Dt} = \mathbf{L}^p \mathbf{F}^p. \tag{A 14a-c}$$

We assume that the plastic flow, \mathbf{L}^p , is symmetric such that,

$$\mathbf{D}^e = \text{sym}(\mathbf{L}^e), \quad \mathbf{W}^e = \mathbf{W}_s, \quad \mathbf{D}^p = \text{sym}(\mathbf{L}^p), \quad \mathbf{W}^p = \mathbf{0}. \tag{A 15a-d}$$

The right polar decomposition of the elastic deformation is defined as $\mathbf{F}^e = \mathbf{R}^e \mathbf{U}^e$, with \mathbf{R}^e the orthogonal rotation tensor and \mathbf{U}^e the symmetric positive definite elastic stretch tensor. The right Cauchy–Green tensor is then, $\mathbf{C}^e = \mathbf{U}^{e2} = \mathbf{F}^{e\top} \mathbf{F}^e$. Since \mathbf{U}^e is symmetric and positive definite, it admits a spectral decomposition which we use to define the logarithmic strain tensor, \mathbf{E}^e ,

$$\mathbf{U}^e = \sum_{i=1}^3 \lambda_i \mathbf{r}_i \otimes \mathbf{r}_i, \quad \text{and} \quad \mathbf{E}^e = \ln(\mathbf{U}^e) \equiv \sum_{i=1}^3 \ln(\lambda_i) \mathbf{r}_i \otimes \mathbf{r}_i, \tag{A 16a,b}$$

where $\{\lambda_i\}$ are the principal stretches, $\{\mathbf{r}_i\}$ are the right principal directions and each $\lambda_i > 0$. Further we define the volumetric Jacobians as,

$$J \equiv \det(\mathbf{F}) > 0, \quad J^e \equiv \det(\mathbf{F}^e) > 0, \quad J^p \equiv \det(\mathbf{F}^p) > 0. \tag{A 17a–c}$$

We introduce the solid phase volumetric free energy, φ_s , which is defined as,

$$\varphi_s = J^e \bar{\rho}_s \psi_s, \quad \text{such that} \quad \varphi_s = \hat{\varphi}_s(\mathbf{C}^e) = \tilde{\varphi}_s(\mathbf{E}^e). \tag{A 18a,b}$$

Therefore (A 11) has the following specialized form,

$$\begin{aligned} & \left(\tilde{\boldsymbol{\sigma}} - 2J^{e-1} \mathbf{F}^e \frac{\partial \hat{\varphi}_s(\mathbf{C}^e)}{\partial \mathbf{C}^e} \mathbf{F}^{e\top} \right) : \mathbf{D}^e + (\tilde{\boldsymbol{\sigma}} : (\mathbf{F}^e \mathbf{D}^p \mathbf{F}^{e-1}) - (J^{e-1} \varphi_s \mathbf{1}) : \mathbf{D}^p) \\ & - \frac{n}{\rho_f} \frac{D^f \rho_f}{Dt} \left(p_f - \rho_f^2 \frac{\partial \hat{\psi}_f(\rho_f)}{\partial \rho_f} \right) + (\boldsymbol{\tau}_f : \mathbf{D}_{0f}) + \mathbf{f}_d \cdot (\mathbf{v}_s - \mathbf{v}_f) \geq 0. \end{aligned} \tag{A 19}$$

A.6. Rules for constitutive relations

The expression in (A 19) must be true for all flows everywhere. Since it is possible to conceive of mixture motions with independently varying (and possibly vanishing) values for \mathbf{D}^e , \mathbf{D}^p , $D^s \rho_f / Dt$, \mathbf{D}_{0f} and $(\mathbf{v}_s - \mathbf{v}_f)$, the following relations must each individually be satisfied,

$$p_f - \rho_f^2 \frac{\partial \hat{\psi}_f(\rho_f)}{\partial \rho_f} = 0 \tag{A 20}$$

$$\boldsymbol{\tau}_f : \mathbf{D}_{0f} \geq 0 \tag{A 21}$$

$$\tilde{\boldsymbol{\sigma}} - 2J^{e-1} \mathbf{F}^e \frac{\partial \hat{\varphi}_s(\mathbf{C}^e)}{\partial \mathbf{C}^e} \mathbf{F}^{e\top} = 0 \tag{A 22}$$

$$\tilde{\boldsymbol{\sigma}} : (\mathbf{F}^e \mathbf{D}^p \mathbf{F}^{e-1}) - (J^{e-1} \varphi_s \mathbf{1}) : \mathbf{D}^p \geq 0 \tag{A 23}$$

$$\mathbf{f}_d \cdot (\mathbf{v}_s - \mathbf{v}_f) \geq 0. \tag{A 24}$$

Appendix B

Following the thermodynamic analysis in appendix A, we let the solid phase effective granular stress be given by a stiff elastic specialization of the model derived in Anand & Su (2005).

B.1. Solid phase effective granular stress

Beginning with the equality in (A 22), we define the solid phase effective stress $\tilde{\sigma}$ as,

$$\tilde{\sigma} = 2J^{e-1} \mathbf{F}^e \frac{\partial \hat{\varphi}_s(\mathbf{C}^e)}{\partial \mathbf{C}^e} \mathbf{F}^{e\top}. \tag{B 1}$$

We then define the elastic stress measure, \mathbf{T}^e , such that,

$$\mathbf{T}^e = J^e \mathbf{F}^{e\top} \tilde{\sigma} \mathbf{F}^{e-1}, \quad \text{and} \quad \tilde{\sigma} = J^{e-1} \mathbf{F}^{e-1\top} \mathbf{T}^e \mathbf{F}^{e\top}. \tag{B 2a,b}$$

Combining these expressions, we also have,

$$\mathbf{T}^e = 2\mathbf{C}^e \frac{\partial \hat{\varphi}_s(\mathbf{C}^e)}{\partial \mathbf{C}^e} = \frac{\partial \tilde{\varphi}_s(\mathbf{E}^e)}{\partial \mathbf{E}^e}. \tag{B 3}$$

We choose the volumetric free energy function, $\tilde{\varphi}_s(\mathbf{E}^e) = G \|\mathbf{E}_0^e\|^2 + (1/2)K \text{tr}(\mathbf{E}^e)^2$, with G the solid shear modulus and K the solid bulk modulus with units of stress. The elastic stress measure is therefore given by,

$$\mathbf{T}^e = \mathcal{C}[\mathbf{E}^e] \equiv 2G\mathbf{E}_0^e + K \text{tr}(\mathbf{E}^e)\mathbf{1}. \tag{B 4}$$

B.2. Solid phase plastic strain rate

The solid phase plastic flow rate, \mathbf{D}^p , must obey the inequality in (A 23). By substituting the expression from (B 2) into this inequality, we find,

$$\mathbf{T}^e : \mathbf{D}^p - \varphi_s \mathbf{1} : \mathbf{D}^p \geq 0. \tag{B 5}$$

We let the granular skeleton of the mixture be elastically stiff, such that $\mathbf{U}^e \approx \mathbf{1}$, $J^e \approx 1$ and $\mathbf{E}^e \ll \mathbf{1}$. In this limit, (A 23) is dominated by the stiff plastic dissipation,

$$\mathcal{D} \equiv \mathbf{T}^e : \mathbf{D}^p \geq 0. \tag{B 6}$$

We introduce another measure of the plastic strain rate, $\tilde{\mathbf{D}}^p$, defined as follows,

$$\tilde{\mathbf{D}}^p = \mathbf{F}^e \mathbf{D}^p \mathbf{F}^{e-1}, \quad \text{such that} \quad \mathbf{D}_s = \mathbf{D}^e + \tilde{\mathbf{D}}^p. \tag{B 7a,b}$$

And therefore, (B 6) becomes,

$$\mathcal{D} = \tilde{\sigma} : \tilde{\mathbf{D}}^p \geq 0. \tag{B 8}$$

To satisfy the dissipation inequality in (B 6), we define the plastic strain rate \mathbf{D}^p implicitly via $\tilde{\mathbf{D}}^p$ defined in (2.26) subject to (B 8).

Appendix C

In this section we describe the specific details of the numerical implementation referenced in § 4.

C.1. Material point method discretization

The material point method, as first derived by Sulsky, Chen & Schreyer (1994), is a numerical scheme for solving dynamic problems in solid mechanics where materials undergo large deformations. The basic algorithm defined in Sulsky *et al.* (1994) and generalized by Bardenhagen & Kober (2004) involves discretizing material fields (such as density and stress) on a set of material point tracers and solving the equations of motion on a background grid.

In Abe *et al.* (2013) and Bandara & Soga (2015), the material point method is extended to solve the equations of mixtures defined in Jackson (2000) (here in (2.13) and (2.14)). The algorithm presented in this work derives directly from the weak formulation of the governing equations in table 3 and differs slightly from prior works (due to different simplifying assumptions).

C.1.1. Definition of material point tracers

As shown in figure 7(c), the two continuum bodies defined in figure 2 by \mathcal{B}_s^t and \mathcal{B}_f^t are discretized into material blocks represented by discrete material points. We let the continuum representation of the bodies be given by,

$$\sum_{p=1}^{N_s} U_{sp}(\mathbf{x}, t) = \begin{cases} 1 & \mathbf{x} \in \mathcal{B}_s^t \\ 0 & \text{else} \end{cases} \quad \sum_{p=1}^{N_f} U_{fp}(\mathbf{x}, t) = \begin{cases} 1 & \mathbf{x} \in \mathcal{B}_f^t \\ 0 & \text{else,} \end{cases} \quad (C\ 1a,b)$$

where \mathbf{x} is the position vector in the domain Ω , t is time, $U_{sp}(\mathbf{x}, t)$ and $U_{fp}(\mathbf{x}, t)$ are the p th material point characteristic functions (as in Bardenhagen & Kober (2004)) that are co-moving with the material and N_s and N_f are the number of solid and fluid material point tracers respectively. Intuitively, the sum of the phase-wise characteristic functions defines a spatial field which is equal to 1 within the body and 0 outside.

We construct the solid continuum fields using the U_{sp} functions with $\bar{\rho}_s(\mathbf{x})$ defined at time t^k by the N_s coefficients $\{\bar{\rho}_{sp}^k\}$ and $\tilde{\sigma}(\mathbf{x})$ by the N_s coefficients $\{\tilde{\sigma}_p^k\}$. The fluid continuum fields are constructed using U_{fp} such that the fields $\bar{\rho}_f(\mathbf{x})$, $\rho_f(\mathbf{x})$, $\boldsymbol{\tau}_f(\mathbf{x})$, and $p_f(\mathbf{x})$ are given at time t^k by the N_f coefficients $\{\bar{\rho}_{fp}^k\}$, $\{\rho_{fp}^k\}$, $\{\boldsymbol{\tau}_{fp}^k\}$, and $\{p_{fp}^k\}$ respectively.

We also introduce a measure of material point weights, v_{sp}^k and v_{fp}^k , with,

$$v_{sp}^k = \int_{\Omega} U_{sp}(\mathbf{x}, t^k) dv, \quad v_{fp}^k = \int_{\Omega} U_{fp}(\mathbf{x}, t^k) dv. \quad (C\ 2a,b)$$

Each material point has a centroid (centre of mass) which maps to a location \mathbf{x}_{sp} for the p th solid material point and \mathbf{x}_{fp} for the p th fluid material point. This centroid moves through the domain and has an associated momentum (at time t^k) given by $m_{sp}\mathbf{v}_{sp}^k$ or $m_{fp}\mathbf{v}_{fp}^k$ respectively with,

$$m_{sp} = v_{sp}^k \bar{\rho}_{sp}^k, \quad m_{fp} = v_{fp}^k \bar{\rho}_{fp}^k \quad (C\ 3a,b)$$

and $\{m_{sp}\}$, $\{m_{fp}\}$ constant but not necessarily uniform.

C.1.2. Definition of background grid basis

In addition to the material point representation of the continuum bodies, we also use a grid to solve the weak form equations of motion and for approximating material fields (for post-processing and simplifying intermediate calculations). Since both

bodies live within the same computational domain, Ω , we let one discrete grid serve this purpose for the entire mixture. The grid is defined by a set of continuous nodal basis functions,

$$\sum_{i=1}^{[n]} \mathcal{N}_i(\mathbf{x}) = 1 \quad \forall \mathbf{x} \in \Omega, \tag{C 4}$$

where $\mathcal{N}_i(\mathbf{x})$ is the i th nodal basis function and $[n]$ is the total number of nodes (or degrees of freedom if discontinuous shape functions are used). With this definition we can then define the nodal fields $\mathbf{a}_s(\mathbf{x})$, $\mathbf{v}_s(\mathbf{x})$, $\mathbf{a}_f(\mathbf{x})$, $\mathbf{v}_f(\mathbf{x})$ and $n(\mathbf{x})$ at time t^k by the $[n]$ coefficients $\{\mathbf{a}_{s_i}^k\}$, $\{\mathbf{v}_{s_i}^k\}$, $\{\mathbf{a}_{f_i}^k\}$, $\{\mathbf{v}_{f_i}^k\}$, $\{n_i^k\}$ respectively.

In addition to the fields above, we also introduce a measure of the nodal basis weight, V_i ,

$$V_i = \int_{\Omega} \mathcal{N}_i(\mathbf{x}) \, dv. \tag{C 5}$$

It is numerically convenient to let the background grid be composed of regular Cartesian elements. We therefore let the construction of the basis functions $\{\mathcal{N}_i(\mathbf{x})\}$ be the tensor product of 1-D functions $\mathcal{N}_{1D}(\hat{x}_{ij})$ with \hat{x}_{ij} a measure of the distance from the i th grid node to the spatial position \mathbf{x} along the j th primary Cartesian direction, $\{\hat{x}_1, \hat{x}_2, \hat{x}_3\}$.

$$\mathcal{N}_i(\mathbf{x}) = \prod_{j=1}^{DIM} \mathcal{N}_{1D}(\hat{x}_{ij}), \tag{C 6}$$

where DIM is the dimension of the simulation. The choice of $\mathcal{N}_{1D}(\hat{x}_{ij})$ can have significant impact on the accuracy of the material point method, especially for reduction of ‘grid-crossing’ error (see Bardenhagen & Kober (2004)) and quadrature error (see Steffen, Kirby & Berzins (2008)). In this work we use adjusted cubic splines based on those presented in Steffen *et al.* (2008).

C.2. Time-marching procedure

The weak forms of the governing equations are solved according to the following explicit procedure (shown in figure 22) to step from time t^k to time t^{k+1} where,

$$t^{k+1} = \hat{t}^k + \Delta t. \tag{C 7}$$

- (i) The discrete material point states of the two phases are known at time t^k .

$$\left. \begin{array}{l} \text{solid phase: } \{ \bar{\rho}_{sp}^k, \tilde{\sigma}_p^k, m_{sp}, \mathbf{x}_{sp}^k, \mathbf{v}_{sp}^k \} \\ \text{fluid phase: } \{ \bar{\rho}_{fp}^k, \rho_{fp}^k, \boldsymbol{\tau}_{fp}^k, p_{fp}^k, m_{fp}, \mathbf{x}_{fp}^k, \mathbf{v}_{fp}^k \}. \end{array} \right\} \tag{C 8}$$

- (ii) The material point centroids, $\{\mathbf{x}_{sp}^k\}$ and $\{\mathbf{x}_{fp}^k\}$ are used to generate the mapping coefficients $\{\mathcal{S}_{sip}^k\}$, $\{\mathcal{S}_{fip}^k\}$, $\{\nabla \mathcal{S}_{sip}^k\}$ and $\{\nabla \mathcal{S}_{fip}^k\}$.

$$\left. \begin{array}{l} \mathcal{S}_{sip}^k = \mathcal{N}_i(\mathbf{x}_{sp}^k), \quad \nabla \mathcal{S}_{sip}^k = \text{grad}(\mathcal{N}_i(\mathbf{x}))|_{\mathbf{x}_{sp}^k} \\ \mathcal{S}_{fip}^k = \mathcal{N}_i(\mathbf{x}_{fp}^k), \quad \nabla \mathcal{S}_{fip}^k = \text{grad}(\mathcal{N}_i(\mathbf{x}))|_{\mathbf{x}_{fp}^k}. \end{array} \right\} \tag{C 9}$$

- (iii) The nodal mass coefficients, $\{m_{si}^k\}$ and $\{m_{fi}^k\}$, are determined.

$$m_{si}^k = \sum_{p=1}^{N_s} m_{sp} \mathcal{S}_{sip}^k, \quad m_{fi}^k = \sum_{p=1}^{N_f} m_{fp} \mathcal{S}_{fip}^k. \tag{C 10a,b}$$

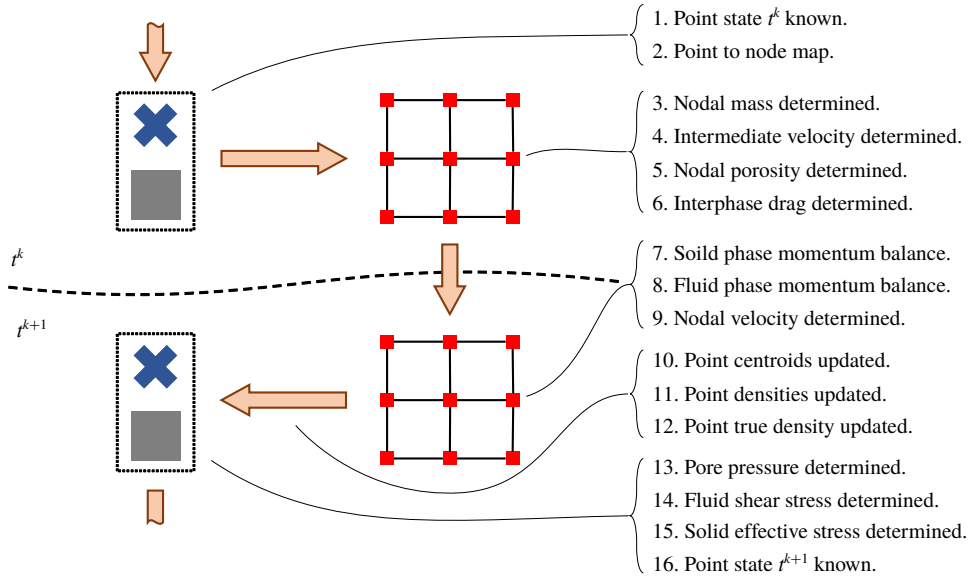


FIGURE 22. (Colour online) The explicit time integration procedure described in § C.2 is shown. At the beginning of the step, the material points carry the full state of the mixture. The mixture state is then mapped from the points to the background grid nodes, where the equations of motion are solved according to the weak form of momentum balance. At the end of the step, the solved equations of motion are used to update the mixture state on the material points.

- (iv) An intermediate nodal representation of the phase velocity fields, given by the coefficients $\{\mathbf{v}_{si}^*\}$ and $\{\mathbf{v}_{fi}^*\}$, is determined by approximating the material point velocity fields, given by the coefficients $\{\mathbf{v}_{sp}^k\}$ and $\{\mathbf{v}_{fp}^k\}$.

$$m_i^k \mathbf{v}_{si}^* = \sum_{p=1}^{N_s} m_{sp} \mathbf{v}_{sp}^k S_{sip}^k, \quad m_{fi}^k \mathbf{v}_{fi}^* = \sum_{p=1}^{N_f} m_{fp} \mathbf{v}_{fp}^k S_{fip}^k. \tag{C 11a,b}$$

- (v) The nodal porosity coefficients, $\{n_i^k\}$, are determined.

$$n_i^k = 1 - \frac{m_{si}^k}{V_i \rho_s}. \tag{C 12}$$

- (vi) The nodal approximation of the inter-phase drag, given by $\{\mathbf{f}_{di}^*\}$, is determined.

$$\mathbf{f}_{di}^* = \frac{18n_i^k(1-n_i^k)\eta_0}{d^2} \hat{F}((1-n_i^k), Re_i^*)(\mathbf{v}_{si}^* - \mathbf{v}_{fi}^*) \sum_{p=1}^{N_f} v_{fp}^k S_{fip}^k \tag{C 13}$$

$$Re_i^* = \frac{n_i^k \|\mathbf{v}_{si}^* - \mathbf{v}_{fi}^*\| d}{\eta_0}. \tag{C 14}$$

- (vii) The acceleration of the solid phase at time t^{k+1} , given by $\{\mathbf{a}_{si}^{k+1}\}$, is determined.

$$m_{si}^k \mathbf{a}_{si}^{k+1} = m_{si}^k \mathbf{g} - \mathbf{f}_{di}^k - \sum_{p=1}^{N_s} (v_{sp}^k \tilde{\sigma}_p^k \nabla S_{sip}^k) + (1-n_i^k) \sum_{p=1}^{N_f} (v_{fp}^k p_{fp}^k \nabla S_{fip}^k) + \mathbf{s}_{si}^k$$

(\mathbf{s}_{si}^k is a boundary condition enforced on the i th node). (C 15)

(viii) The acceleration of the fluid phase at time t^{k+1} , given by $\{\mathbf{a}_{f_i}^{k+1}\}$, is determined.

$$m_{f_i}^k \mathbf{a}_{f_i}^{k+1} = m_{f_i}^k \mathbf{g} + \mathbf{f}_{d_i}^k - \sum_{p=1}^{N_f} (\mathbf{v}_{f_p}^k \boldsymbol{\tau}_{f_p}^k \nabla \mathcal{S}_{f_p}^k) + n_i^k \sum_{p=1}^{N_f} (\mathbf{v}_{f_p}^k p_{f_p}^k \nabla \mathcal{S}_{s_{ip}}^k) + \mathbf{s}_{f_i}^k$$

($\mathbf{s}_{f_i}^k$ is a boundary condition enforced on the i th node). (C 16)

(ix) The phase velocity fields at time t^{k+1} , given by $\{\mathbf{v}_{s_i}^{k+1}\}$ and $\{\mathbf{v}_{f_i}^{k+1}\}$, are determined explicitly according to,

$$\mathbf{v}_{s_i}^{k+1} = \mathbf{v}_{s_i}^* + \Delta t \mathbf{a}_{s_i}^{k+1}, \quad \mathbf{v}_{f_i}^{k+1} = \mathbf{v}_{f_i}^* + \Delta t \mathbf{a}_{f_i}^{k+1}. \tag{C 17a,b}$$

(x) The material point centroid positions and velocities are updated explicitly as in Brackbill & Ruppel (1986) and Brackbill, Kothe & Ruppel (1988),

$$\left. \begin{aligned} \mathbf{x}_{s_p}^{k+1} &= \mathbf{x}_{s_p}^k + \Delta t \sum_{i=1}^{[n]} \mathbf{v}_{s_i}^{k+1} \mathcal{S}_{s_{ip}}^k + (\boldsymbol{\delta}_{s_p}^k), & \mathbf{v}_{s_p}^{k+1} &= \mathbf{v}_{s_p}^k + \Delta t \sum_{i=1}^{[n]} \mathbf{a}_{s_i}^{k+1} \mathcal{S}_{s_{ip}}^k \\ \mathbf{x}_{f_p}^{k+1} &= \mathbf{x}_{f_p}^k + \Delta t \sum_{i=1}^{[n]} \mathbf{v}_{f_i}^{k+1} \mathcal{S}_{f_{ip}}^k + (\boldsymbol{\delta}_{f_p}^k), & \mathbf{v}_{f_p}^{k+1} &= \mathbf{v}_{f_p}^k + \Delta t \sum_{i=1}^{[n]} \mathbf{a}_{f_i}^{k+1} \mathcal{S}_{f_{ip}}^k \end{aligned} \right\} \tag{C 18}$$

where $\boldsymbol{\delta}_{s_p}^{k+1}$ and $\boldsymbol{\delta}_{f_p}^{k+1}$ are the δ position correction described in § C.4.5.

(xi) The material point densities at time t^{k+1} , $\{\bar{\rho}_s^{k+1}\}$ and $\{\bar{\rho}_f^{k+1}\}$, are updated.

$$\left. \begin{aligned} \bar{\rho}_{s_p}^{k+1} &= \bar{\rho}_{s_p}^k \exp \left(-(\Delta t) \text{tr} \left(\sum_{i=1}^{[n]} \mathbf{v}_{s_i}^{k+1} \otimes \nabla \mathcal{S}_{s_{ip}}^k \right) \right) \\ \bar{\rho}_{f_p}^{k+1} &= \bar{\rho}_{f_p}^k \exp \left(-(\Delta t) \text{tr} \left(\sum_{i=1}^{[n]} \mathbf{v}_{f_i}^{k+1} \otimes \nabla \mathcal{S}_{f_{ip}}^k \right) \right) \end{aligned} \right\} \tag{C 19}$$

where \otimes is the tensor product operator.

(xii) The fluid phase material point true densities, $\{\rho_{f_p}^{k+1}\}$, are determined. (Note that for numerical stability, we do not require that $\{n_p^{k+1}\}$, $\{\bar{\rho}_{f_p}^{k+1}\}$, and $\{\rho_{f_p}^{k+1}\}$ be consistent.)

$$n_p^{k+1} = \sum_{i=1}^{[n]} n_i^k \mathcal{S}_{f_{ip}}^k \tag{C 20}$$

$$\rho_{f_p}^{k+1} = \rho_{f_p}^k \exp \left(- \left(\frac{\Delta t}{n_p^{k+1}} \right) \text{tr} \left(\sum_{i=1}^{[n]} [(1 - n_i^k) \mathbf{v}_{s_i}^{k+1} + n_i^k \mathbf{v}_{f_i}^{k+1}] \otimes \nabla \mathcal{S}_{f_{ip}}^k \right) \right). \tag{C 21}$$

(xiii) The fluid phase material point pore pressure state is determined directly from the true fluid density.

$$p_{f_p}^{k+1} = \kappa \ln \left(\frac{\rho_{f_p}^{k+1}}{\rho_{0f}} \right). \tag{C 22}$$

(xiv) The fluid phase material point shear stresses, $\{\boldsymbol{\tau}_{fp}^{k+1}\}$, are determined directly from the fluid phase velocity gradient.

$$\left. \begin{aligned} \boldsymbol{\tau}_{fp}^{k+1} &= 2\eta_0 \left(1 + \frac{5}{2}(1 - n_p^{k+1}) \right) \mathbf{D}_{0fp}^{k+1} \\ \mathbf{D}_{fp}^{k+1} &= \text{sym} \left(\sum_{i=1}^{[n]} \mathbf{v}_{fi}^{k+1} \otimes \nabla \mathcal{S}_{fip}^k \right). \end{aligned} \right\} \quad (\text{C } 23)$$

(xv) The solid phase material point effective stresses, $\{\tilde{\boldsymbol{\sigma}}_p^{k+1}\}$, are determined with a semi-implicit method described in § C.3.

$$\begin{aligned} \tilde{\boldsymbol{\sigma}}_p^{k+1} &= \tilde{\boldsymbol{\sigma}}_p^k + \Delta t [2G(\mathbf{D}_{0sp}^{k+1} - (\tilde{\mathbf{D}}_0^p)^{k+1}) \\ &\quad + K \text{tr}(\mathbf{D}_{sp}^{k+1} - (\tilde{\mathbf{D}}^p)^{k+1}) \mathbf{1} + \mathbf{W}_{sp}^{k+1} \tilde{\boldsymbol{\sigma}}_p^k - \tilde{\boldsymbol{\sigma}}_p^k \mathbf{W}_{sp}^{k+1}]. \end{aligned} \quad (\text{C } 24)$$

(xvi) The discrete material point states of the two phases are known for time t^{k+1} ,

$$\left. \begin{aligned} \text{solid phase: } &\{\tilde{\rho}_{sp}^{k+1}, \tilde{\boldsymbol{\sigma}}_p^{k+1}, m_{sp}, \mathbf{x}_{sp}^{k+1}, \mathbf{v}_{sp}^{k+1}\} \\ \text{fluid phase: } &\{\tilde{\rho}_{fp}^{k+1}, \rho_{fp}^{k+1}, \boldsymbol{\tau}_{fp}^{k+1}, p_{fp}^{k+1}, m_{fp}, \mathbf{x}_{fp}^{k+1}, \mathbf{v}_{fp}^{k+1}\} \end{aligned} \right\} \quad (\text{C } 25)$$

and the procedure is repeated for the $k + 1$ time step.

C.3. Semi-implicit effective stress algorithm

The solid phase material point effective stress is updated at each time step with the semi-implicit time integration scheme described in this section. Given the material point stress states at time t^k , $\{\tilde{\boldsymbol{\sigma}}_p^k\}$, and the total material point flow rates at time t^{k+1} ,

$$\mathbf{D}_{sp}^{k+1} = \text{sym}(\mathbf{L}_{sp}^{k+1}), \quad \mathbf{W}_{sp}^{k+1} = \text{skw}(\mathbf{L}_{sp}^{k+1}), \quad \mathbf{L}_{sp}^{k+1} = \sum_{i=1}^{[n]} \mathbf{v}_{fi}^{k+1} \otimes \nabla \mathcal{S}_{fip}^k \quad (\text{C } 26a-c)$$

we solve for the plastic flow rates $\{(\tilde{\mathbf{D}}^p)^{k+1}\}$ given by,

$$(\tilde{\mathbf{D}}^p)^{k+1} = \frac{(\dot{\gamma}^p)_p^{k+1}}{\sqrt{2}} \frac{\tilde{\boldsymbol{\sigma}}_0^p{}^{k+1}}{\|\tilde{\boldsymbol{\sigma}}_0^p{}^{k+1}\|} + \frac{1}{3} (\beta(\dot{\gamma}^p)_p^{k+1} + (\dot{\xi}_1)_p^{k+1} + (\dot{\xi}_2)_p^{k+1}) \mathbf{1} \quad (\text{C } 27)$$

such that (with $(\dot{\gamma}^p)_p^{k+1}$, $(\dot{\xi}_1)_p^{k+1}$, and $(\dot{\xi}_2)_p^{k+1}$ determined for each material point) the material point stress state at time t^{k+1} is given by (C 24).

C.3.1. Definition of trial stress

The update from (C 24) can be separated into a trial step,

$$\tilde{\boldsymbol{\sigma}}_p^{tr} = \tilde{\boldsymbol{\sigma}}_p^k + \Delta t [2G\mathbf{D}_{0sp}^{k+1} + K \text{tr}(\mathbf{D}_{sp}^{k+1}) \mathbf{1} + \mathbf{W}_{sp}^{k+1} \tilde{\boldsymbol{\sigma}}_p^k - \tilde{\boldsymbol{\sigma}}_p^k \mathbf{W}_{sp}^{k+1}] \quad (\text{C } 28)$$

and a plastic step,

$$\tilde{\boldsymbol{\sigma}}_p^{k+1} = \tilde{\boldsymbol{\sigma}}_p^{tr} - \Delta t [2G(\tilde{\mathbf{D}}_0^p)^{k+1} + K \text{tr}((\tilde{\mathbf{D}}^p)^{k+1}) \mathbf{1}], \quad (\text{C } 29)$$

where $\tilde{\boldsymbol{\sigma}}_p^{tr}$ is a trial stress found between times t^k and t^{k+1} . Since the trial stress given in (C 28) is an explicit function of the strain rates in (C 29), we use it as the starting point of our implicit algorithm for solving (C 29).

C.3.2. Simplification to scalar relation

The expression in (C 29) is separable into a deviatoric part and isotropic part,

$$\tilde{\sigma}_{0_p}^{k+1} = \tilde{\sigma}_{0_p}^{tr} - 2G\Delta t(\tilde{\mathbf{D}}_0^p)^{k+1}, \quad \text{tr}(\tilde{\sigma}_p^{k+1}) = \text{tr}(\tilde{\sigma}_p^{tr}) - 3K\Delta t \text{tr}((\tilde{\mathbf{D}}^p)^{k+1}). \quad (\text{C } 30a,b)$$

The following scalar stress measures reduce the implicit tensor relations above to a set of implicit scalar relations (which are much simpler to solve numerically),

$$\bar{\tau}_p^{tr} = \frac{\|\tilde{\sigma}_{0_p}^{tr}\|}{\sqrt{2}}, \quad \bar{\tau}_p^{k+1} = \frac{\|\tilde{\sigma}_p^{k+1}\|}{\sqrt{2}}, \quad \tilde{p}_p^{tr} = -\frac{1}{3}\text{tr}(\tilde{\sigma}_p^{tr}), \quad \tilde{p}_p^{k+1} = -\frac{1}{3}\text{tr}(\tilde{\sigma}_p^{k+1}) \quad (\text{C } 31a-d)$$

and therefore (C 29) becomes,

$$\bar{\tau}_p^{k+1} = \bar{\tau}_p^{tr} - G\Delta t (\dot{\gamma}^p)_p^{k+1} \quad (\text{C } 32)$$

$$\tilde{p}_p^{k+1} = \tilde{p}_p^{tr} + K\Delta t(\beta(\dot{\gamma}^p)_p^{k+1} + (\dot{\xi}_1)_p^{k+1} + (\dot{\xi}_2)_p^{k+1}). \quad (\text{C } 33)$$

By solving the system of equations in (C 32) and (C 33) subject to the following discrete yield conditions,

$$\left. \begin{aligned} (f_1)_p^{k+1} &= \bar{\tau}_p^{k+1} - \max((\mu_p + \beta)\tilde{p}_p^{k+1}, 0) \\ (f_1)_p^{k+1} &\leq 0, \quad (\dot{\gamma}^p)_p^{k+1} \geq 0, \quad (f_1)_p^{k+1}(\dot{\gamma}^p)_p^{k+1} = 0 \\ (f_2)_p^{k+1} &= -\tilde{p}_p^{k+1} \\ (f_2)_p^{k+1} &\leq 0, \quad (\dot{\xi}_1)_p^{k+1} \geq 0, \quad (f_2)_p^{k+1}(\dot{\xi}_1)_p^{k+1} = 0 \\ (f_3)_p^{k+1} &= g(\phi)\tilde{p}_p^{k+1} - (a\phi)^2[(\dot{\gamma}^p)_p^{k+1} - K_4(\dot{\xi}_2)_p^{k+1}]^2 d^2 \rho_s + 2\eta_0((\dot{\gamma}^p)_p^{k+1} - K_4(\dot{\xi}_2)_p^{k+1}) \\ (f_3)_p^{k+1} &\leq 0, \quad (\dot{\xi}_2)_p^{k+1} \leq 0, \quad (f_3)_p^{k+1}(\dot{\xi}_2)_p^{k+1} = 0 \end{aligned} \right\} \quad (\text{C } 34)$$

we arrive at the final effective granular stresses at time t^{k+1} ,

$$\tilde{\sigma}_p^{k+1} = \frac{\bar{\tau}_p^{k+1}}{\bar{\tau}_p^{tr}} \tilde{\sigma}_{0_p}^{tr} - \tilde{p}_p^{k+1} \mathbf{1}. \quad (\text{C } 35)$$

C.3.3. Complete algorithm for stress update

To solve the system of equations from § C.3.2, we use the procedure described in algorithm 1 to successively project the trial stress state defined by $\{\tilde{p}_p^{tr}\}$ and $\{\bar{\tau}_p^{tr}\}$ to the yield surfaces given in (C 34). As shown in figure 23, once an admissible stress update is found, the algorithm exits and proceeds to the next time step. In our implementation of this procedure, we choose to use a simple Newton iteration scheme to solve for each of the projections.

C.4. Specific notes about implementation

In this section we briefly discuss the implementation of the boundary conditions, contact forces, partial saturation and what we call the δ position correction.

C.4.1. Kinematic boundary conditions

The kinematic boundary condition used in this work is inherited from that used by Dunatunga & Kamrin (2015). In this method, the boundary force vectors, $\mathbf{s}_{s_i}^k$ and $\mathbf{s}_{f_i}^k$, on the boundary nodes are determined such that some prescribed velocity is achieved at the end of the explicit time step.

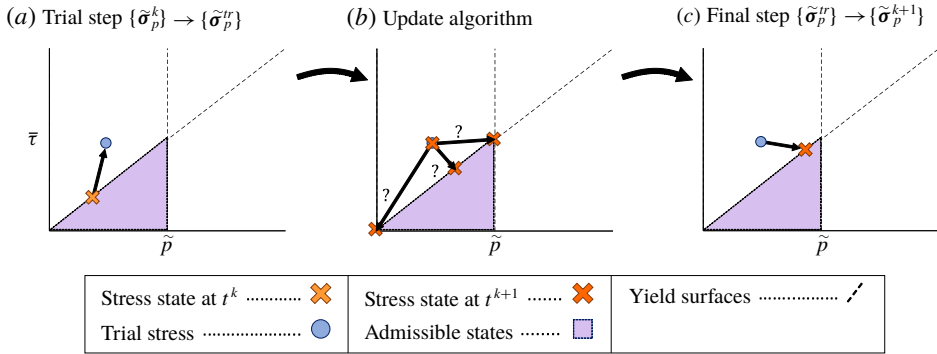


FIGURE 23. (Colour online) The basic solid phase effective stress update proceeds as follows. (a) A trial step is taken from the stress state at time t^k assuming that all flow is elastic. (b) The method described in algorithm 1 is used to determine how to project the trial stress to an admissible stress state. (c) The final stress state is updated from the trial stress state.

Algorithm 1 Outline of stress update procedure

- 1: **procedure** STRESS UPDATE
- 2: Determine trial state.
- 3: Check if trial stress is admissible (if so, **exit**).
- 4: Solve assuming final stress is on f_2 yield surface
- 5: Check if solved state is admissible (if so, **exit**).
- 6: Solve assuming final stress is on f_1 yield surface only.
- 7: Check if solved state is admissible (if so, **exit**).
- 8: Solve assuming final stress is on f_1 and f_3 yield surfaces.
- 9: This state must be admissible, so **exit**.
- 10: **end procedure**

C.4.2. Mixed boundary conditions

In some simulations, we implement a frictional boundary condition on the solid phase. For these simulations, only the component of \mathbf{v}_{sp}^{k+1} normal to the boundary is prescribed (and therefore, the normal component of \mathbf{s}_{si}^k is also determined). We then let the tangential force component be given by either a no-slip condition or,

$$\mathbf{s}_{si}^k - (\mathbf{s}_{si}^k \cdot \mathbf{n}_{bi})\mathbf{n}_{bi} = -\mu_1 \left\| \sum_{p=1}^{N_s} (v_{sp} \tilde{p}_p^k \nabla \mathcal{S}_{sip}) \right\| \frac{\mathbf{v}_{si}^* - (\mathbf{v}_{si}^* \cdot \mathbf{n}_{bi})\mathbf{n}_{bi}}{\|\mathbf{v}_{si}^* - (\mathbf{v}_{si}^* \cdot \mathbf{n}_{bi})\mathbf{n}_{bi}\|} \tag{C 36}$$

whichever is smaller, where \mathbf{n}_{bi} is the boundary normal at the i th node.

C.4.3. Contact algorithm

In some of the qualitative results presented in this work, we implement the contact algorithm from Huang *et al.* (2011). This algorithm calculates an explicit inter-body force (when a third material body is introduced) which enforces a frictional, non-penetrating contact between the third body and each of the two phases presented in this work.

C.4.4. Partial immersion

In the parts of the solid body where there is no fluid, we say that the viscosity, η_0 , is zero. Numerically we accomplish this by constructing a nodal viscosity field at each time step given by the coefficients $\{\eta_{0i}^k\}$. We then let the value of η_0 in § C.2 be determined on each solid phase material point by, $\{\eta_{0p}^k\}$ where,

$$\eta_{0i}^k = \begin{cases} \eta_0 & \text{if } m_{fi}^k > 0 \\ 0 & \text{if } m_{fi}^k = 0 \end{cases} \quad \forall i \in [1, [n]], \quad \eta_{0p}^k = \sum_{i=1}^{[n]} \eta_{0i}^k \mathcal{S}_{sip} \quad \forall p \in [1, N_s]. \quad (\text{C } 37a,b)$$

C.4.5. Dynamic quadrature error reduction

Particle methods for simulating fluid flows have an inherent problem with (among other things) point clumping (see recent work by Koh, Gao & Luo (2012) and Maljaars (2016)). There are many physically admissible flows, such as those with stagnation points, which will result in material point tracers gathering together. By choosing the material point centroids as the quadrature points for our integral approximations, this clumping leads to significant quadrature error. In some fluid simulations, we see extremely spurious flows develop, which we attribute to this quadrature error.

To address this issue, we have developed a novel approach which ‘nudges’ material point centroids as the material flows. This nudge is the δ_{sp}^k and δ_{fp}^k from (C 18). The method we introduce relies on the nodal weight measure from (C 5) (which is known *a priori*). Since our material point characteristic functions are partitions of unity within the body (by C 1), we have,

$$V_i = \sum_{p=1}^{N_s} \int_{\Omega} \mathcal{N}_i(\mathbf{x}) U_{\alpha p}(\mathbf{x}) \, dv \quad \text{if } (\mathcal{N}_i(\mathbf{x}) = 0 \text{ for } \mathbf{x} \notin \mathcal{B}'_{\alpha}), \quad (\text{C } 38)$$

where α is a more general notation for either s or f .

We determine how much quadrature error has accumulated by using the material point weights and centroids as quadrature points for the above integral and measure the relative overshoot error, e_{si} and e_{fi} , as follows,

$$v_{\alpha i} \equiv \sum_{p=1}^{N_{\alpha}} v_{\alpha p} \mathcal{N}_i(\mathbf{x}_{\alpha p}), \quad e_{\alpha i} = \max \left(0, \frac{v_{\alpha i} - V_i}{V_i} \right). \quad (\text{C } 39a,b)$$

We have attempted several methods of reducing this error (which will be explored in a future work); however the method used in this work is a strain-rate-dependent position correction given as follows,

$$\delta_{\alpha p}^k = -\lambda \Delta t (\Delta x)^2 \| \mathbf{L}_{\alpha 0 p}^{k+1} \| \sum_{i=1}^{[n]} e_{\alpha i} \nabla \mathcal{S}_{\alpha ip}, \quad (\text{C } 40)$$

with Δx the grid spacing of the Cartesian grid and λ an arbitrary scale factor.

REFERENCES

- ABE, K., SOGA, K. & BANDARA, S. 2013 Material point method for coupled hydromechanical problems. *J. Geotech. Geoenviron. Engng* **140** (3), 04013033.
- ALLEN, B. & KUDROLLI, A. 2017 Depth resolved granular transport driven by shearing fluid flow. *Phys. Rev. Fluids* **2** (2), 024304.
- AMARSID, L., DELENNE, J. Y., MUTABARUKA, P., MONERIE, Y., PERALES, F. & RADJAI, F. 2017 Viscoinertial regime of immersed granular flows. *Phys. Rev. E* **96**, 012901.
- ANAND, L. & SU, C. 2005 A theory for amorphous viscoplastic materials undergoing finite deformations, with applications to metallic glasses. *J. Mech. Phys. Solids* **53** (6), 1362–1396.
- BANDARA, S. & SOGA, K. 2015 Coupling of soil deformation and pore fluid flow using material point method. *Comput. Geotech.* **63**, 199–214.
- BARDENHAGEN, S. G. & KOBER, E. M. 2004 The generalized interpolation material point method. *Comput. Model. Engng Sci.* **5** (6), 477–496.
- BEETSTRA, R., VAN DER HOEF, M. A. & KUIPERS, J. A. M. 2007 Drag force of intermediate Reynolds number flow past mono- and bidisperse arrays of spheres. *AIChE J.* **53** (2), 489–501.
- BOYER, F., GAUZELLI, E. & POULIQUEN, O. 2011 Unifying suspension and granular rheology. *Phys. Rev. Lett.* **107** (18), 188301.
- BRACKBILL, J. U. & RUPPEL, H. M. 1986 Flip: a method for adaptively zoned, particle-in-cell calculations of fluid flows in two dimensions. *J. Comput. Phys.* **65** (2), 314–343.
- BRACKBILL, J. U., KOTHE, D. B. & RUPPEL, H. M. 1988 Flip: a low-dissipation, particle-in-cell method for fluid flow. *Comput. Phys. Commun.* **48** (1), 25–38.
- CARMAN, P. C. 1937 Fluid flow through granular beds. *Trans. Inst. Chem. Engrs* **15**, 150–166.
- CASSAR, C., NICOLAS, M. & POULIQUEN, O. 2005 Submarine granular flows down inclined planes. *Phys. Fluids* **17** (10), 103301.
- CECCATO, F., BEUTH, L., VERMEER, P. A. & SIMONINI, P. 2016 Two-phase material point method applied to the study of cone penetration. *Comput. Geotech.* **80**, 440–452.
- CECCATO, F. & SIMONINI, P. 2016 Granular flow impact forces on protection structures: Mpm numerical simulations with different constitutive models. *Proc. Engng* **158**, 164–169.
- CHANG, C. & POWELL, R. L. 1993 Dynamic simulation of bimodal suspensions of hydrodynamically interacting spherical particles. *J. Fluid Mech.* **253**, 1–25.
- CHANG, C. & POWELL, R. L. 1994 Effect of particle size distributions on the rheology of concentrated bimodal suspensions. *J. Rheol.* **38** (1), 85–98.
- CHONG, J. S., CHRISTIANSEN, E. B. & BAER, A. D. 1971 Rheology of concentrated suspensions. *J. Appl. Polym. Sci.* **15** (8), 2007–2021.
- CLIFT, R., GRACE, J. R. & WEBER, M. E. 2005 *Bubbles, Drops, and Particles*. Courier Corporation.
- COOK, B. K., NOBLE, D. R. & WILLIAMS, J. R. 2004 A direct simulation method for particle-fluid systems. *Engng Comput.* **21** (2/3/4), 151–168.
- COUSSY, O. 2004 *Poromechanics*. Wiley.
- DA CRUZ, F., EMAM, S., PROCHNOW, M., ROUX, J.-N. & CHEVOIR, F. 2005 Rheophysics of dense granular materials: discrete simulation of plane shear flows. *Phys. Rev. E* **72** (2), 021309.
- DRUMHELLER, D. S. 2000 On theories for reacting immiscible mixtures. *Intl J. Engng Sci.* **38**, 347–382.
- DUNATUNGA, S. & KAMRIN, K. 2015 Continuum modelling and simulation of granular flows through their many phases. *J. Fluid Mech.* **779**, 483–513.
- DUPUIT, J. É. J. 1863 *Études théoriques et pratiques sur le mouvement des eaux dans les canaux découverts et à travers les terrains perméables: avec des considérations relatives au régime des grandes eaux, au débouché à leur donner, et à la marche des alluvions dans les rivières à fond mobile*. Dunod.
- EINSTEIN, A. 1906 Calculation of the viscosity-coefficient of a liquid in which a large number of small spheres are suspended in irregular distribution. *Ann. Phys. Leipzig* **19**, 286–306.
- FERN, E. J. & SOGA, K. 2016 The role of constitutive models in mpm simulations of granular column collapses. *Acta Geotech.* **11** (3), 659–678.

- GURTIN, M. E., FRIED, E. & ANAND, L. 2010 *The Mechanics and Thermodynamics of Continua*. Cambridge University Press.
- HENANN, D. L. & KAMRIN, K. 2013 A predictive, size-dependent continuum model for dense granular flows. *Proc. Natl Acad. Sci.* **110** (17), 6730–6735.
- VAN DER HOEF, M. A., BEETSTRA, R. & KUIPERS, J. A. M. 2005 Lattice-Boltzmann simulations of low-Reynolds-number flow past mono- and bidisperse arrays of spheres: results for the permeability and drag force. *J. Fluid Mech.* **528**, 233–254.
- HOUSSAIS, M., ORTIZ, C. P., DURIAN, D. J. & JEROLMACK, D. J. 2015 Onset of sediment transport is a continuous transition driven by fluid shear and granular creep. *Nat. Commun.* **6**, 6527.
- HUANG, P., ZHANG, X., MA, S. & HUANG, X. 2011 Contact algorithms for the material point method in impact and penetration simulation. *Intl J. Numer. Meth. Engng* **85** (4), 498–517.
- JACKSON, R. 2000 *The Dynamics of Fluidized Particles*. Cambridge University Press.
- JOP, P., FORTERRE, Y. & POULIQUEN, O. 2006 A constitutive law for dense granular flows. *Nature* **441** (7094).
- KAMRIN, K. & HENANN, D. L. 2015 Nonlocal modeling of granular flows down inclines. *Soft Matt.* **11** (1), 179–185.
- KAMRIN, K. & KOVAL, G. 2012 Nonlocal constitutive relation for steady granular flow. *Phys. Rev. Lett.* **108** (17), 178301.
- KLIKA, V. 2014 A guide through available mixture theories for applications. *Critical Rev. Solid State Mater. Sci.* **39** (2), 154–174.
- KOH, C. G., GAO, M. & LUO, C. 2012 A new particle method for simulation of incompressible free surface flow problems. *Intl J. Numer. Methods Engng* **89** (12), 1582–1604.
- MALJAARS, J. M. 2016 A hybrid particle-mesh method for simulating free surface flows. Delft University of Technology.
- MAST, C. M., MACKENZIE-HELNWEIN, P., ARDUINO, P., MILLER, G. R. & SHIN, W. 2012 Mitigating kinematic locking in the material point method. *J. Comput. Phys.* **231** (16), 5351–5373.
- PAILHA, M. & POULIQUEN, O. 2009 A two-phase flow description of the initiation of underwater granular avalanches. *J. Fluid Mech.* **633**, 115–135.
- POSLINSKI, A. J., RYAN, M. E., GUPTA, R. K., SESHADRI, S. G. & FRECHETTE, F. J. 1988 Rheological behavior of filled polymeric systems ii. The effect of a bimodal size distribution of particulates. *J. Rheol.* **32** (8), 751–771.
- RONDON, L., POULIQUEN, O. & AUSSILLOUS, P. 2011 Granular collapse in a fluid: role of the initial volume fraction. *Phys. Fluids* **23** (7), 073301.
- ROUX, S. & RADJAI, F. 1998 Texture-dependent rigid-plastic behavior. In *Physics of Dry Granular Media* (ed. H. J. Herrmann, J. P. Hovi & S. Luding), pp. 229–236. Springer.
- ROUX, S. & RADJAI, F. 2001 Statistical approach to the mechanical behavior of granular media. In *Mechanics for a New Millennium* (ed. H. Aref & J. W. Phillips), pp. 181–196. Kluwer.
- RUDNICKI, J. W. & RICE, J. R. 1975 Conditions for the localization of deformation in pressure-sensitive dilatant materials. *J. Mech. Phys. Solids* **23** (6), 371–394.
- SHAPIRO, A. P. & PROBSTEIN, R. F. 1992 Random packings of spheres and fluidity limits of monodisperse and bidisperse suspensions. *Phys. Rev. Lett.* **68** (9), 1422–1425.
- SOGA, K., ALONSO, E., YERRO, A., KUMAR, K. & BANDARA, S. 2015 Trends in large-deformation analysis of landslide mass movements with particular emphasis on the material point method. *Geotechnique* **66** (3), 248–273.
- STEFFEN, M., KIRBY, R. M. & BERZINS, M. 2008 Analysis and reduction of quadrature errors in the material point method (mpm). *Intl J. Numer. Meth. Engng* **76** (6), 922–948.
- STICKEL, J. J. & POWELL, R. L. 2005 Fluid mechanics and rheology of dense suspensions. *Annu. Rev. Fluid Mech.* **37**, 129–149.
- STORMS, R. F., RAMARAO, B. V. & WEILAND, R. H. 1990 Low shear rate viscosity of bimodally dispersed suspensions. *Powder Technol.* **63** (3), 247–259.

- SULSKY, D., CHEN, Z. & SCHREYER, H. L. 1994 A particle method for history-dependent materials. *Comput. Meth. Appl. Mech. Engng* **118** (1–2), 179–196.
- TRUESDELL, C. & NOLL, W. 1965 *The Non-Linear Field Theories of Mechanics*. Springer.
- TURIAN, R. M. & YUAN, T.-F. 1977 Flow of slurries in pipelines. *AIChE J.* **23** (3), 232–243.
- WILMANSKI, K. 2008 *Continuum Thermodynamics – Part 1: Foundations*. World Scientific.
- ZHAO, Y. & DAVIS, R. H. 2002 Interaction of two touching spheres in a viscous fluid. *Chem. Engng Sci.* **57** (11), 1997–2006.